A Rational Approach to Characterize Fracture Properties of Composites to Support a Cohesive Zone Material Model

by

Mohammed Raihan

A Thesis Presented in Partial Fulfillment
of the Requirements for the Degree
Master of Science

Approved April 2023 by the
Graduate Supervisory Committee:

Subramaniam Rajan, Chair
Narayanan Neithalath
Christian Hoover
Ravi Kiran Yellavajjala

ARIZONA STATE UNIVERSITY

May 2023

ABSTRACT

Composites are replacing conventional materials in aerospace applications due to their light weight, non-corrosiveness, and high specific strength. This thesis aims to characterize the input data for IM7-8552 unidirectional composite to support MAT213, an orthotropic elasto-plastic damage material model and MAT_186, a mixed mode cohesive zone model used to model delamination. MAT_213 in conjunction with MAT_186 can be used to predict the behavior of composite under crush and impact loads including delamination. MAT_213 requires twelve sets of stress-strain curves, direction-dependent material constants, and flow rule coefficients as input. All the necessary inputs are obtained through the post-processing of a total of twelve distinct quasi-static and room temperature (QS-RT) experiments. MAT_186 is driven by a set of Mode I and Mode II fracture parameters and traction separation laws, a constitutive law that derives the relationship between stresses and relative displacements at integration points of cohesive elements. Obtaining cohesive law parameters experimentally is a tedious process as it requires close monitoring of the crack length during the test, which is a difficult task to achieve with accuracy even after using sophisticated equipment such as Digital Image Correlation (DIC). In this thesis, a numerical inverse analysis method to precisely predict these parameters by using finite element analysis with cohesive zone modeling and response surface methodology (RSM) is proposed. Three steps comprise RSM. The process in Step 1 involves calculating the root mean square error between the finite element and experimental load-displacement curves to produce the response surface. In step 2, the response surface is fitted with a second-order polynomial using the Levenberg-Marquardt algorithm. In step 3, an optimization problem is solved by

minimizing the fitted function to find the optimum cohesive zone parameters. Finally, the obtained input for MAT_213 and MAT_186 material models is validated by performing a quasi-isotropic tension test simulation.

DEDICATION

This thesis is dedicated to my parents, Naveed Ahmed, and Shaher Banu, for their constant support and affection throughout my academic career.

ACKNOWLEDGMENTS

I express my immense gratitude to my thesis supervisor, Dr. Subramaniam Rajan for his endless patience, invaluable guidance, and support during my pursuit of a master's degree at Arizona State University. Under his wisdom and mentorship, I have grown into a better individual. I would also like to thank my committee members, Dr. Narayanan Neithalath, Dr. Christian Hoover, and Dr. Ravi Yellavajjala, for the teachings they have provided me. I would like to give special acknowledgment to Ashutosh Maurya for his exceptional guidance and mentorship throughout the process. Finally, I would like to thank my friends and colleagues at ASU.

TABLE OF CONTENTS

Page

CHAPTER Page

LIST OF TABLES

LIST OF FIGURES

Figure Page

Figure Page

Figure Page

Figure Page

1. INTRODUCTION

1.1. BACKGROUND AND LITERATURE REVIEW

Composite materials have become increasingly popular over the past few decades, as they possess a range of unique properties, including high specific strength, non-corrosiveness, stiffness, and fatigue resistance, which make them superior to conventional materials. In the aerospace industry, composites are extensively used to manufacture airplane fuselages, wings, and engine components. Similarly, in the automotive industry, they are employed in the production of car bodies, chassis, and other structural components. The sporting goods industry also utilizes composite materials to create items such as tennis rackets, golf clubs, and bicycle frames, taking advantage of their exceptional strength and light weight. Additionally, composite materials are used in the medical industry to manufacture prosthetics and implants, owing to their biocompatibility, strength, and stiffness. Wind energy also benefits from composite materials, with wind turbine blades being constructed from these materials due to their light weight and high strength, which results in efficient energy production. Moreover, composites offer several advantages, including design flexibility, resistance to corrosion, and lower maintenance costs. Even though composites have attractive features, the use of composites is limited. One of the reasons is – composites when used in structural systems such as aerospace and automotive are subjected to variety of loading conditions. Among these, impact loading conditions are the most critical. Under impact loads composites undergo deformation, damage, and failure. All these components influence the future response of the composite. Therefore, there is a need for a numerical tool to predict the

behavior of composites under impact and crush loadings. Under the joint effort of NASA and FAA a generalized orthotropic elasto-plastic damage material model (OEPDMM) is developed and implemented in a commercial transient dynamic finite element software LS-DYNA as MAT_213. This material model is driven completely by experimental data. One key feature of MAT_213 is that it allows the user the flexibility to define how material behaves since the input to this material model is given in a tabular form. MAT_213 has three sub-models-deformation, damage, and failure. Along with predicting linear deformations, MAT_213 can also predict non-linear deformations, damage, and failure. The required input to drive deformation, damage and failure include twelve sets of stress-strain curves, direction-dependent material constants, and flow rule coefficients. All the necessary inputs are obtained through the post-processing of a total of 12 distinct quasi-static and room temperature (QS-RT) experiments. This thesis provides a framework to generate MAT_213 input data for IM7-8552 unidirectional carbon/epoxy composite.

Along with deformations, composites sustain significant internal damage when subjected to impact and crush loads. This internal damage is primarily the result of delamination caused by high normal, tangential stresses and stress concentrations generated by impact loads. This causes the interfaces of the laminate to de-bond. Delamination significantly reduces the structure's stiffness and strength. Moreover, it cannot be visually inspected because it occurs in the inter laminar layers. Understanding the mechanisms of delamination in composite laminates is therefore essential for preventing catastrophic structural failure. Therefore, in recent decades, a significant amount of focus has been placed on the development of models to predict delamination. There are three different

modes in delamination, including mode I or opening mode, mode II or shearing mode, and mode III or tearing mode. Among these damage modes, mode I, mode II and mixed mode (derived from combination of mode I and mode II) are the most commonly occurring delamination modes in laminated composited. Various numerical modeling techniques like Virtual Crack Closing Technique (VCCT), Extended Finite Element Method, Multiscale Reduced Order Modeling (ROM), Random Lattice Method (RLM), and Cohesive Zone Modeling (CZM) can be used for modeling delamination. L. F.Alessandro Fascetti [1] discusses each one of these methods highlighting their salient features, advantages, challenges and applications in detail. Because of its low computational time and accuracy, CZM has been widely used and is most effective in modeling delamination in laminated composite materials. Moreover, CZM is relatively easy to implement, and it is incorporated in almost all commercial finite element software. LS-DYNA, a nonlinear transient dynamic finite element code, is used in our current study to build and analyze finite element models. LS-DYNA's MAT186, a mixed mode cohesive zone model was used to model delamination.

The cohesive zone model is governed by the traction separation law (TSL), a constitutive law that derives the relationship between stresses and relative displacements at integration points of cohesive elements. Generally, traction separation law is defined by using two or more fracture parameters. The number of parameters is dictated by the shape of the traction separation law, which in turn is determined by the type of interface fracture mechanism. Peak traction (σ_{max}), critical energy release rate (G_C), also known as fracture toughness, and penalty stiffness (k) are three parameters shared by all TSLs. Figure. 1.1 shows a simple bilinear traction separation law. The x and y axis of the

traction separation law represents stress (σ) and displacement (δ) respectively, while the area under the curve represents the fracture energy (G_C). A general traction separation law consists of three stages. The initial, undamaged linear region of the first stage has a stiffness (k) on the order of 10^6 – 10^7 N/mm^2. These range of values are selected to provide reliable results [2], [3]. The subsequent softening stages are damage initiation and evolution. Damage initiation indicates when the damage evolution begins, which occurs after maximum traction is attained. Damage evolution describes the rate at which the composite's stiffness degrades [4]. Linear, multilinear, exponential, trapezoidal, and tabular softening curves are used based on the experience of an analyst performing fracture simulations to match the experimental load displacement curve or by predicting the shape by determining the mechanism of fracture and how the material behaves while conducting fracture tests on the specimens. N. Dourado et al. [2] utilized bilinear cohesive law (BCL) to characterize mode II delamination for two carbon/epoxy composites. The Bilinear cohesive laws obtained were quite different for both the composites. A trapezoidal law with bilinear cohesive law was used by M.F.S.F. de Moura et al.[3] to characterize fracture properties for mode II loading of a hybrid laminate. They assumed this shape of the law to account for the ductile behavior observed during the experiments. S.M. Jensen et al. [5] characterized multilinear cohesive law for mode I delamination in a glass epoxy unidirectional composite. J.C.S. Azevedo et al. [6] employed linear cohesive laws to identify mode II delamination behavior of three different adhesive joints.

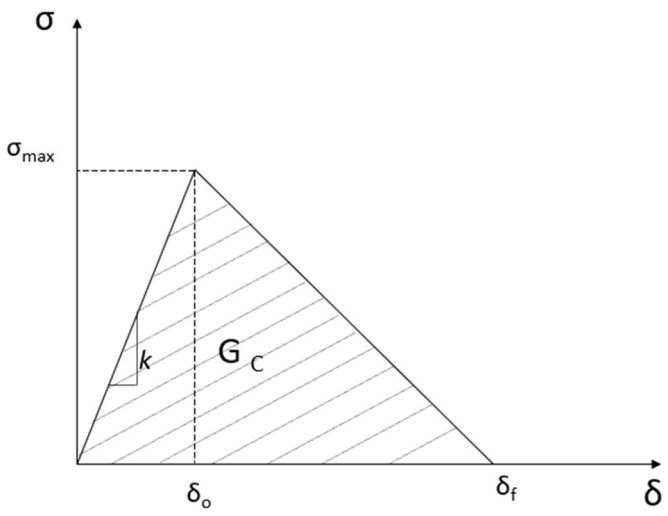

Figure 1.1: General Bi-linear Traction Separation Law

Various researchers have used various methods to characterize the traction separations law parameters. Double cantilever beam (DCB) test is typically used by many researchers to characterize mode I cohesive law parameters ([4], [7], [8], [9]). While mode II fracture properties are characterized by using end notched flexure (ENF) ([2], [3], [6], [7]). Using DCB and ENF test data both mode I and mode II critical energy release rates can be computed directly. However, obtaining other parameters shown in Figure. 1.1 is often difficult and typically determined by calibration of finite element models with experimental results. Some researchers have characterized these properties completely from the DCB and ENF experimental data ([7],[10]). Some researchers have used analytical techniques [11], or inverse methods ([2], [5], [12], [13]) by comparing the FE model results with experimental results by tuning the cohesive law parameters. In this work both mode I and mode II cohesive law parameters are obtained by using DCB and ENF finite element model along with the experimental load-displacement result from DCB and ENF coupon tests. Response surface methodology (RSM) and optimization

techniques are employed to obtain both optimal mode I and mode II fracture properties and traction separation laws.

1.2. THESIS OBJECTIVES

There is a need for a robust numerical model to predict the behavior of composite materials subjected to impact and crush loadings seen in aerospace applications. OEPDMM, generalized orthotropic composite tabulated plasticity damage material model is implemented in LS-DYNA ®, a commercially available nonlinear transient dynamic finite element code as MAT_213. MAT_213 can be used to simulate deformation, damage and failure in composite materials. MAT_213 is restricted to model composite lamina and not the interlaminar zone present in composite materials. However, MAT_213 in conjunction with a cohesive zone model can be used to build representative finite element models. The interlaminar zone is constructed by connecting the composite laminas by cohesive zone elements (CZE). MAT_213 offers flexibility to the analyst as all of the required input is provided in the form of tabulated data which includes twelve sets of stress-strain curves, direction-dependent material constants, and flow rule coefficients. All the necessary inputs are obtained through the post-processing of a total of 12 distinct quasi-static and room temperature (QS-RT) experiments. MAT_186, a cohesive zone material model in LS-DYNA is utilized to model the interlaminar zone. MAT_186 is driven by traction separation law, which describes the tractions that develop in the element as a function of deformation. The thesis focuses on the procedures to generate input data for MAT213 and MAT186 for a unidirectional composite material IM7-8552. The primary objectives are presented below.

1. Use the experimental results from tests performed on IM7-8552 unidirectional carbon fiber/epoxy resin composite to generate the input cards for MAT_213 material model.
2. Perform single and multi-element finite element verification test simulations to match the experimental stress-strain input curves and to ensure compatibility and proper functioning of MAT_213.
3. Use DCB and ENF finite element models along with the response surface methodology to get the optimal mode I and mode II fracture properties and traction separation laws.
4. Perform a quasi-isotropic tension test simulation using the generated input for MAT_213 and MAT_186 and compare the simulation results with the experimental results in order to validate the characterized input.

2. MAT_213 OVERVIEW AND COHESIVE ZONE MODEL

MAT_213 is an orthotropic elasto-plastic material model (OEPDMM) material model available in LS-DYNA ®, a commercially available nonlinear transient dynamic finite element code suitable for impact and crush simulations. The material model has three key components: deformation, damage, and failure. The deformation sub-model captures both linear and nonlinear deformations using classical plasticity formulation. The damage sub-model considers the decrease in the material's elastic stiffness as plastic strain increases. The failure sub-model predicts when the material loses its load-carrying capacity. The OEPDMM approach relies exclusively on tabulated experimental data from material characterization tests that are physically meaningful. The data includes stress-strain curves at various temperatures and strain rates for the deformation sub-model, damage parameter-total strain curves for the damage sub-model, and failure data for different failure theories used in the computer code to drive the failure sub-model. The material model has several features, such as tension/compression asymmetry, temperature effects, strain rate effects, and stochastic variation of material properties. Table 1.1 presents a comparison between MAT_213 and other material models in LS-DYNA, highlighting the key features of each. Full details about the theory and development of MAT_213 can be found in articles by several authors ([14], [15], [16], [17], [18], [19], [13], [20]). An abbreviated summary of the MAT_213 material model theory is presented in this chapter.

Table 1 Comparison of MAT213 Key Features with Other Material Models in LS-DYNA.

Table taken from [21]. (✓ = Included, ✗ = Not Included, and ✹ = Partially Included)

MAT	Tabulated Input	Tension/Compression Asymmetry	Plasticity	Solid Element	Shell Element	Damage Model	In-built Failure Model	Rate Effects	Temperature Effects	Stochastic	Implicit
022	✗	✗	✗	✓	✓	✓	✗	✗	✗	✗	✓
023	✹	✗	✗	✓	✓	✗	✗	✗	✓	✗	✓
054 /55	✗	✗	✗	✓	✓	✓	✓	✓	✗	✗	✗
058	✹	✗	✗	✗	✓	✓	✓	✓	✗	✗	✗
059	✗	✗	✗	✓	✓	✓	✓	✗	✗	✗	✓
116	✗	✗	✗	✓	✓	✗	✓	✗	✗	✗	✗
117	✗	✗	✗	✗	✓	✗	✗	✗	✗	✗	✗
118	✗	✗	✗	✗	✓	✗	✗	✗	✗	✗	✗
158	✗	✗	✗	✗	✓	✓	✓	✓	✗	✗	✗
161/162	✗	✗	✗	✓	✓	✓	✓	✓	✗	✗	✓
213	✓	✓	✓	✓	✓	✓	✓	✓	✓	✓	✗
219	✗	✗	✗	✓	✓	✓	✓	✗	✗	✗	✗
221	✹	✗	✗	✓	✗	✓	✓	✹	✗	✗	✗

2.1. DEFORMATION SUB-MODEL

The deformation sub-model employs classical plasticity theory, with plasticity initiation determined by a general quadratic three-dimensional orthotropic yield function derived from the Tsai-Wu failure model, expressed as:

$$f(\sigma)=a+\begin{pmatrix}F_1 & F_2 & F_3 & 0 & 0 & 0\end{pmatrix}\begin{bmatrix}\sigma_{11}\\ \sigma_{22}\\ \sigma_{33}\\ \sigma_{12}\\ \sigma_{23}\\ \sigma_{31}\end{bmatrix}+\begin{bmatrix}\sigma_{11}\\ \sigma_{22}\\ \sigma_{33}\\ \sigma_{12}\\ \sigma_{23}\\ \sigma_{31}\end{bmatrix}^T\begin{bmatrix}F_{11} & F_{12} & F_{13} & 0 & 0 & 0\\ F_{12} & F_{22} & F_{23} & 0 & 0 & 0\\ F_{13} & F_{23} & F_{33} & 0 & 0 & 0\\ 0 & 0 & 0 & F_{44} & 0 & 0\\ 0 & 0 & 0 & 0 & F_{55} & 0\\ 0 & 0 & 0 & 0 & 0 & F_{66}\end{bmatrix}\begin{bmatrix}\sigma_{11}\\ \sigma_{22}\\ \sigma_{33}\\ \sigma_{12}\\ \sigma_{23}\\ \sigma_{31}\end{bmatrix} \quad (2.1)$$

Where, the stresses in different coordinate directions are denoted by $\left(\sigma_{ij}\right)$. The yield function coefficients (F_i 's and F_{ij} 's) vary depending on the current state of yield stress in each direction. To monitor the changes in yield stresses, the model requires twelve sets of stress-strain curves, including tension and comp ression tests in the 1, 2, and 3 directions, as well as shear and off-axis tension or compression tests in the 1-2, 2-3, and 3-1 planes.

Yield function coefficients corresponding to principal material directions and principal material planes are determined as the function of yield stresses which are given by:

$$\begin{aligned}
F_1&=\frac{1}{\sigma_{11}^T}-\frac{1}{\sigma_{11}^C} & F_{11}&=\frac{1}{\sigma_{11}^T\sigma_{11}^C} & F_{44}&=\frac{1}{\sigma_{12}^2}\\
F_2&=\frac{1}{\sigma_{22}^T}-\frac{1}{\sigma_{22}^C} & F_{22}&=\frac{1}{\sigma_{22}^T\sigma_{22}^C} & F_{55}&=\frac{1}{\sigma_{23}^2}\\
F_3&=\frac{1}{\sigma_{33}^T}-\frac{1}{\sigma_{33}^C} & F_{33}&=\frac{1}{\sigma_{33}^T\sigma_{33}^C} & F_{66}&=\frac{1}{\sigma_{31}^2}
\end{aligned} \quad (2.2)$$

In Eq. 2.2, $\left(\sigma_{ij}\right)$ are the current values of yield stresses in the normal and shear directions. T and C denote tensile and compressive yield stress respectively. The off-axis coefficients can be computed from 45° tests in various coordinate directions and are given as

$$F_{12} = \frac{2}{\left(\sigma_{12}^{45}\right)^2} - \frac{F_1 + F_2}{\sigma_{12}^{45}} - \frac{1}{2}\left(F_{11} + F_{22} + F_{44}\right) \tag{2.3}$$

$$F_{23} = \frac{2}{\left(\sigma_{23}^{45}\right)^2} - \frac{F_2 + F_3}{\sigma_{23}^{45}} - \frac{1}{2}\left(F_{22} + F_{33} + F_{55}\right) \tag{2.4}$$

$$F_{13} = \frac{2}{\left(\sigma_{31}^{45}\right)^2} - \frac{F_1 + F_3}{\sigma_{31}^{45}} - \frac{1}{2}\left(F_{11} + F_{33} + F_{66}\right) \tag{2.5}$$

F_{12} is derived from the 45° off-axis tension test conducted in the 1-2 plane. Similarly, F_{23} and F_{13} can be determined by performing 45° off-axis tests in the 2-3 and 1-3 planes, respectively. A non-associative flow rule is used to compute the evolution of components of plastic strains which is given as:

$$d\boldsymbol{\varepsilon}^p = d\lambda \frac{\partial h}{\partial \boldsymbol{\sigma}} \tag{2.6}$$

The plastic potential function for the flow is given as:

$$h = \sqrt{\begin{matrix} H_{11}\sigma_{11}^2 + H_{22}\sigma_{22}^2 + H_{33}\sigma_{33}^2 + 2H_{12}\sigma_{11}\sigma_{22} + 2H_{23}\sigma_{22}\sigma_{33} + \\ 2H_{31}\sigma_{33}\sigma_{11} + H_{44}\sigma_{12}^2 + H_{55}\sigma_{23}^2 + H_{66}\sigma_{13}^2 \end{matrix}} \tag{2.7}$$

Where, $\left(\sigma_{ij}\right)$ are current values of stresses and H_{ij} are the flow rule coefficients that are constants and depend on the ratios of various plastic Poisson's ratios. The simplified plastic potential function along with Eq. 2.6 can be used to relate plastic Poisson's ratios as follows,

$$
\begin{array}{lll}
\sigma_{11} \neq 0 & \sigma_{22} \neq 0 & \sigma_{33} \neq 0 \\
\nu_{12}^{p} = -\dfrac{\dot{\varepsilon}_{22}^{p}}{\dot{\varepsilon}_{11}^{p}} = -\dfrac{H_{12}}{H_{11}} & \nu_{21}^{p} = -\dfrac{\dot{\varepsilon}_{11}^{p}}{\dot{\varepsilon}_{22}^{p}} = -\dfrac{H_{12}}{H_{22}} & \nu_{32}^{p} = -\dfrac{\dot{\varepsilon}_{22}^{p}}{\dot{\varepsilon}_{33}^{p}} = -\dfrac{H_{23}}{H_{33}} \\
\nu_{13}^{p} = -\dfrac{\dot{\varepsilon}_{33}^{p}}{\dot{\varepsilon}_{11}^{p}} = -\dfrac{H_{13}}{H_{11}} & \nu_{23}^{p} = -\dfrac{\dot{\varepsilon}_{33}^{p}}{\dot{\varepsilon}_{22}^{p}} = -\dfrac{H_{23}}{H_{22}} & \nu_{31}^{p} = -\dfrac{\dot{\varepsilon}_{11}^{p}}{\dot{\varepsilon}_{33}^{p}} = -\dfrac{H_{13}}{H_{33}}
\end{array}
\tag{2.9}
$$

The Eq. 2.7 along with the unidirectional tests in the PMD's are useful in developing procedures to characterize the flow rule coefficients. The procedure for characterizing flow rule coefficients for IM7-8552 composite will be discussed in chapter 3.

2.2. DAMAGE SUB-MODEL

Damage model handles the degradation of elastic stiffness prior to failure. The damage model is essential since the non-linear behavior exhibited by fiber reinforced composites materials are due to the combination of both plasticity, handled by deformation sub-model, and microscopic damage which can be noticed by varying unloading moduli. Damage model relates true stress space to effective stress space. True stress space is related directly to what is measured experimentally. Effective stress space is related to undamaged material where all non-linearity is caused by plasticity. The true stress is related to effective stress through a damage tensor M as

$$
\boldsymbol{\sigma} = \mathbf{M} : \boldsymbol{\sigma}^{eff} \tag{2.10}
$$

The full damage tensor is shown in Eq. 2.11. The use of full damage tensor will lead to the prediction of multiaxial stress in effective state a uniaxial stress state is present in the true space. This leads to a non-physical problem. Therefore, a semi coupled directionality tensor is used in the current implementation as shown by Eq. 2.10.

$$\begin{pmatrix}\sigma_{11}\\ \sigma_{22}\\ \sigma_{33}\\ \sigma_{12}\\ \sigma_{23}\\ \sigma_{13}\end{pmatrix}=\begin{bmatrix}M_{11} & M_{12} & M_{13} & M_{14} & M_{15} & M_{16}\\ M_{21} & M_{22} & M_{23} & M_{24} & M_{25} & M_{26}\\ M_{31} & M_{32} & M_{33} & M_{34} & M_{35} & M_{36}\\ M_{41} & M_{42} & M_{43} & M_{44} & M_{45} & M_{46}\\ M_{51} & M_{52} & M_{53} & M_{54} & M_{55} & M_{56}\\ M_{61} & M_{62} & M_{63} & M_{64} & M_{65} & M_{66}\end{bmatrix}\begin{pmatrix}\sigma_{11}^{eff}\\ \sigma_{22}^{eff}\\ \sigma_{33}^{eff}\\ \sigma_{12}^{eff}\\ \sigma_{23}^{eff}\\ \sigma_{13}^{eff}\end{pmatrix} \tag{2.11}$$

$$\begin{pmatrix}\sigma_{11}\\ \sigma_{22}\\ \sigma_{33}\\ \sigma_{12}\\ \sigma_{23}\\ \sigma_{13}\end{pmatrix}=\begin{bmatrix}M_{11} & 0 & 0 & 0 & 0 & 0\\ 0 & M_{22} & 0 & 0 & 0 & 0\\ 0 & 0 & M_{33} & 0 & 0 & 0\\ 0 & 0 & 0 & M_{44} & 0 & 0\\ 0 & 0 & 0 & 0 & M_{55} & 0\\ 0 & 0 & 0 & 0 & 0 & M_{66}\end{bmatrix}\begin{pmatrix}\sigma_{11}^{eff}\\ \sigma_{22}^{eff}\\ \sigma_{33}^{eff}\\ \sigma_{12}^{eff}\\ \sigma_{23}^{eff}\\ \sigma_{13}^{eff}\end{pmatrix} \tag{2.12}$$

The M coefficients are determined by the damage parameters set by the user as input curves where $0 \leq M \leq 1$.

M is related to damage parameters as given in Eq. 2.13.

$$M_{kk} = M_{kk}\left(d_{11}^{kk}, d_{22}^{kk}, d_{33}^{kk}, d_{12}^{kk}, d_{23}^{kk}, d_{13}^{kk}\right) \tag{2.13}$$

Where, d_{ij}^{kl} indicates the damage induced in ij direction has manifested the reduction of stiffness in the kl direction. More information regarding the damage model can be found in [14], [15], [16], [17], [18], [19], [13], [20].

2.3. FAILURE SUB-MODEL

Failure model determines when the element is eroded. There are three different failure models implemented in MAT_213 and can be used one at a time. These are Tsai-Wu Failure Criteria (TWFC), Puck Failure Criteria (PFC) and Generalized Tabulated Failure Criteria (GTFC). The number of parameters required for each of the implemented failure

criteria are different. TWFC and PFC are based on the failure model established by [22] and [23] respectively. The failure states in GTFC are based on strain rather than stress. For each failure state, there are specific failure surfaces that are defined in terms of the equivalent failure strain and failure angle space. Figure. 2.1 shows the in-plane failure surface where $\varepsilon_{IP^{FAIL}}^{eq}$ is the function of failure angle, θ_{IP}. The equivalent failure strain and the failure angle are computed at each time step using Eq. 2.14 and 2.15 respectively. More details about GTFC can be found in [18], [19].

$$\varepsilon_{IP}^{eq} = \sqrt{\varepsilon_{11}^2 + \varepsilon_{22}^2 + 2\varepsilon_{12}^2} \tag{2.14}$$

$$\theta_{IP} = \cos^{-1}\left(\frac{\sigma_{22}}{\sqrt{\sigma_{22}^2 + \sigma_{12}^2}}\right) \tag{2.15}$$

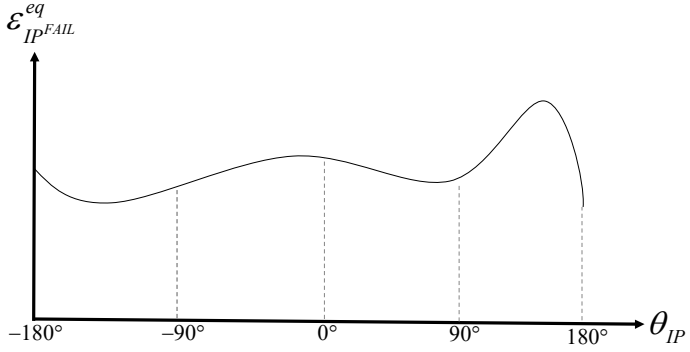

Figure 2.1 General form of In-plane Failure Surface

2.4. COHESIVE ZONE MODEL

The composites materials consist of several laminas bonded together to form a laminate. The interface where two or more laminas are bonded is inherently weaker than the rest of the composite, this makes delamination one of the critical failure modes in composites. When composites are subjected to impact and crush loading, delamination can occur.

Since delamination is essentially the propagation of a crack in a medium, fracture mechanics is an appealing method for describing the phenomenon. Under dynamic loading, the assumptions of linear fracture mechanics (LEFM) [24] are easily violated. Instead, the nonlinear concept of cohesive fracture mechanics, first introduced by Dugdale [25] and Barenblatt [26], can be used. Modeling the interfaces present in composite materials within the framework of finite element (FE) analysis with cohesive zone models (CZM) has made extensive use of the principles of cohesive fracture mechanics. Chapter 1 discusses the literature review for CZM in detail. To summarize CZM allows the analyst to define the interface between composite laminates as a component. The constitutive relationship governing the CZM is in the form of a traction separation law. Figure. 1.1 shows an example of bilinear traction separation law. where $\sigma_{\max}$ is the maximum allowable traction, δ_0 is the separation when softening begins, δ_f is the separation when the material ultimately fails, and *k* is the initial penalty stiffness.

In the current version of MAT_213, there are no provisions for handling interlaminar failure. However, MAT_213 can be used with CZM's or tiebreak contact definitions to accurately predict the composite behavior. In this thesis, MAT_186 is used to model the cohesive zone model. MAT_186 requires an arbitrary shaped normalized traction separation laws as input. The material mode consists of three cohesive formulations for mixed-model interaction that are irreversible in nature. These formulations are distinguished based on the value of the effective separation parameter TES. When TES equals 0, the model follows a power law. When TES equals 1, it adheres to the Benzeggagh-Kenane law. When TES equals 2, a separation parameter is employed to capture the interaction between the relative displacements in the normal (mode I) and

tangential (mode II) directions. The three formulations share a common trait in which the traction separation behavior of the model is primarily determined by certain parameters for normal (mode I) - namely, G_I^C and $\sigma_{\max,I}$, and for tangential (mode II) - namely, G_{II}^C and $\sigma_{\max,II}$ - as well as an arbitrary shaped traction-separation law that applies to both modes. Figure. 2.2 depicts the mixed mode traction separation law.

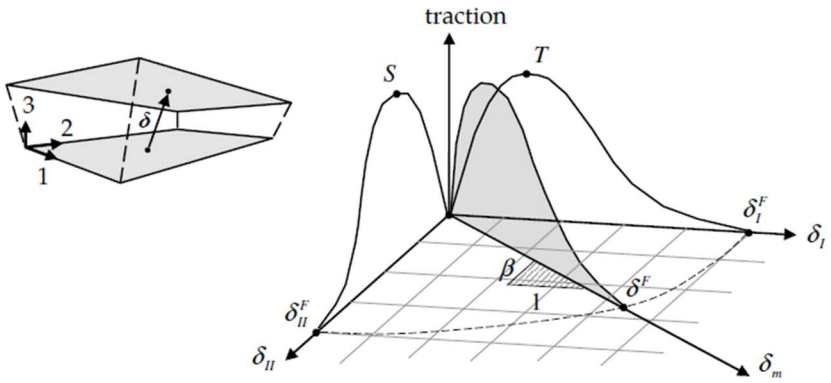

Figure. 2.2. Mixed Mode Traction Separation Law (From LS-Dyna manual volume 2)

The failure separations for both mode I and mode II are calculated using Eq. 2.16 and Eq. 2.17 respectively.

$$\delta_I^F = \frac{G_I^C}{A_{TSLC1}\sigma_{\max,I}} \tag{2.16}$$

$$\delta_{II}^F = \frac{G_{II}^C}{A_{TSLC2}\sigma_{\max,II}} \tag{2.17}$$

Where, A_{TSLC1} denote the area under the traction-separation curve in mode I, and A_{TSLC2} denote the area under the traction-separation curve in mode II. ***Power law*:** In power law, the total mixed mode relative displacement is given as

$\delta_m = \sqrt{\delta_I^2 + \delta_{II}^2}$, where $\delta_I = \delta_3$ is the separation in mode I and $\delta_{II} = \sqrt{\delta_1^2 + \delta_2^2}$ is the separation in the tangential direction.

In this formulation the effective separation parameter TES is set to 0, which means that the interaction between the surfaces follows a power law relationship. The ultimate mixed mode displacement δ^F for power law is given by Eq. 2.18.

$$\delta^F = (1+\beta^2)\left[\left(\frac{A_{TSLC1}\sigma_{\max,I}}{G_I^C}\right)^{XMU} + \left(\frac{A_{TSLC2}\sigma_{\max,II}\beta^2}{G_{II}^C}\right)^{XMU}\right]^{-\frac{1}{XMU}} \tag{2.18}$$

***Benzeggagh-Kenane law*:** In this formulation the effective separation parameter TES is set to 1. The ultimate mixed mode displacement δ^F for power law is given by Eq. 2.19. $\beta = \delta_{II} / \delta_I$ is the mode mixity. Larger the value of XMU, the larger the fracture toughness of mixed mode situations will be.

$$\delta^F = \frac{(1+\beta^2)}{A_{TSLC1}\sigma_{\max,I} + A_{TSLC2}\sigma_{\max,II}\beta^2}\left[G_I^C + \left(G_{II}^C - G_I^C\right)\left(\frac{A_{TSLC2}\sigma_{\max,II}\beta^2}{A_{TSLC1}\sigma_{\max,I} + A_{TSLC2}\sigma_{\max,II}\beta^2}\right)^{XMU}\right] \tag{2.19}$$

3. GENERATION OF MAT_213 INPUT CARDS FOR IM7-8552 COMPOSITE

MAT_213 relies entirely on the data obtained from the experiments as their primary source of input. Table 3.1 has a list of all experiments conducted with unidirectional IM7-8552 composite test coupons to feed data into MAT_213. In order to capture both elastic and plastic deformation, MAT_213 requires 12 sets of stress-strain curves, direction-dependent material constants, and flow rule coefficients as input. All of the necessary inputs are obtained through the post-processing of a total of 12 distinct quasi-static and room temperature (QS-RT) experiments. These experiments include three principal material direction (PMD) tension and compression tests, as well as three principal material plane (PMP) shear and off axis $45°$ tests. For the purpose of determining the IM7-8552 composite's density, a specific gravity test was carried out. Experiments were conducted at ASU, and additional information about test procedures and experimental results is available in [20]. The subsequent sections describe the postprocessing procedures used to generate data for MAT_213 input cards using IM7-8552 experimental results.

Table 2. Summary of Experiment Performed to Characterize Composite IM7-8552 [15].

S.N.	Test Description	ASTM Standard	Resulting Input used to build or calibrate input deck for material model
MAT_213			
1	Tension 1-direction	ASTM D3039	σ_{11}^{T} vs ε_{11}^{T}, $\left(\varepsilon_{11}^{T}\right)_{y}$, ν_{12}, ν_{12}^{p}
2	Tension 2-direction		σ_{22}^{T} vs ε_{22}^{T}, $\left(\varepsilon_{22}^{T}\right)_{y}$, ν_{21}, ν_{21}^{p},
3	Tension 3-direction	_	σ_{33}^{T} vs ε_{33}^{T}, $\left(\varepsilon_{33}^{T}\right)_{y}$, $\nu_{32}, \nu_{31}, \nu_{32}^{p}, \nu_{31}^{p}$
4	Compression 1-direction	ASTM D6641 & ASTM D3410	σ_{11}^{C} vs ε_{11}^{C}, $\left(\varepsilon_{11}^{C}\right)_{y}$
5	Compression 2-direction		σ_{22}^{C} vs ε_{22}^{C}, $\left(\varepsilon_{22}^{C}\right)_{y}$

6	Compression 3-direction	ASTM D7291	σ_{33}^{C} vs ε_{33}^{C}, $\left(\varepsilon_{33}^{C}\right)_y$
7	Shear 1-2 plane	ASTM D5379/D5379 M-12	σ_{12} vs ε_{12}, $\left(\varepsilon_{12}\right)_y$
8	Shear 2-3 plane		σ_{23} vs ε_{23}, $\left(\varepsilon_{23}\right)_y$
9	Shear 1-3 plane		σ_{13} vs ε_{13}, $\left(\varepsilon_{13}\right)_y$
10	Off-axis (45°, 1-2 plane)	ASTM D3039	σ_{12}^{45} vs ε_{12}^{45}, $\left(\varepsilon_{12}^{45}\right)_y$
11	Off-axis (45°, 2-3 plane)	ASTM D7291	σ_{23}^{45} vs ε_{23}^{45}, $\left(\varepsilon_{23}^{45}\right)_y$
12	Off-axis (45°, 1-3 plane)		σ_{13}^{45} vs ε_{13}^{45}, $\left(\varepsilon_{13}^{45}\right)_y$
13	Specific Gravity	ASTM D792-13	$\rho_{composite}$

3.1. GENERATION OF MODEL CURVES

The model curve is an average curve that has been generated by averaging the stress strain results from multiple experimental replicates of a specific test. Model curves were generated for all 12 sets of stress-strain curves. In order to determine the end point of each model curve, the replicate with the lowest total strain value was identified and used as a cut-off point.

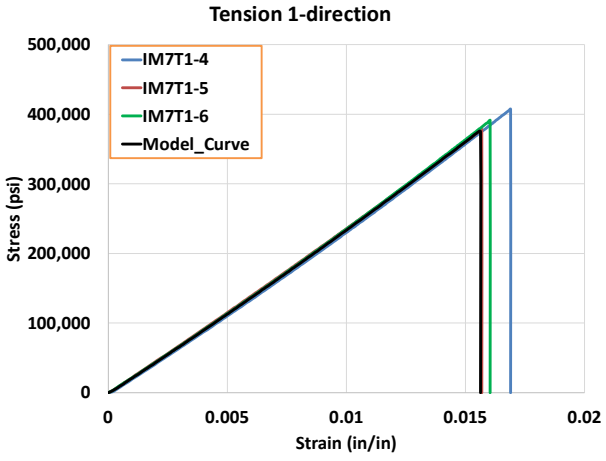

(a)

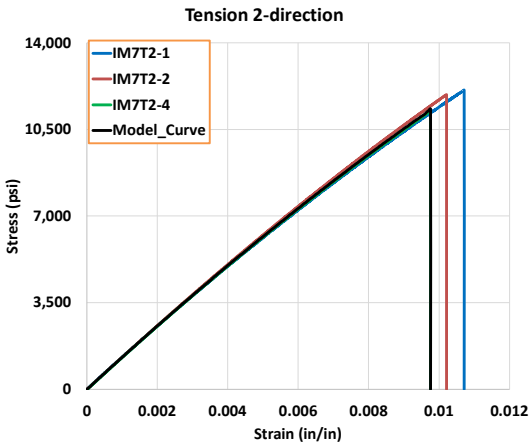

(b)

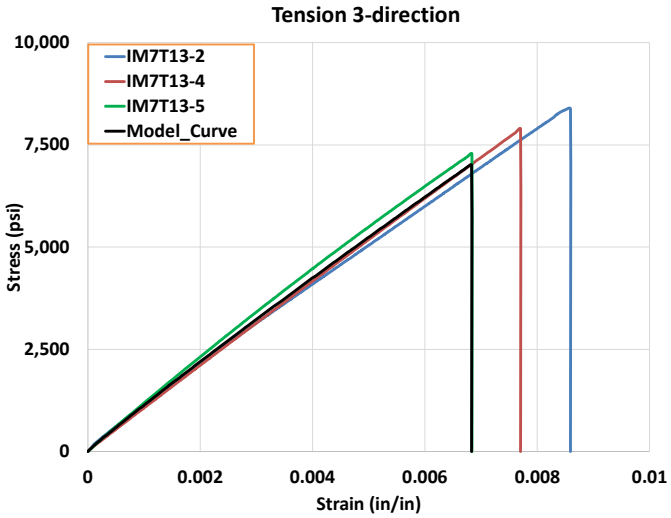

(c)

Figure 3.1. Stress-Strain from Tension Test, (a) 1- direction, (b) 2-direction, and (c) 3-direction.

Figures. 3.1, 3.2, 3.3, 3.4 show all 12 sets of experimental stress strain results and their corresponding model curves. Figure. 3.1 and Figure. 3.2 display stress- strain for three principal material direction tension and compression tests, along with the corresponding model curves. Figure. 3.3 and Figure. 3.4 show stress-strain curves for three principal material plane shear and off-axis tests, respectively. Model curves are represented as solid black lines and are used as tabulated MAT_213 input in all the models utilized in this thesis.

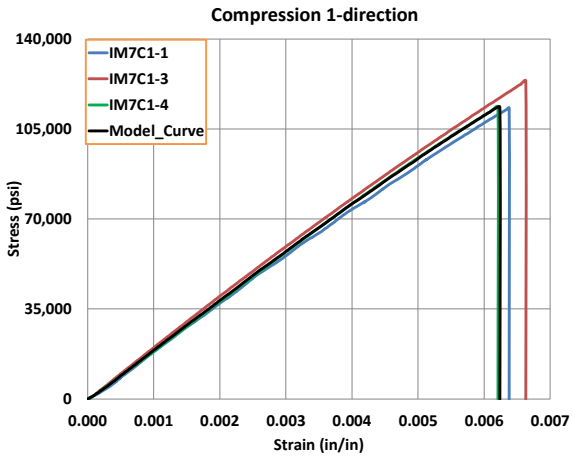

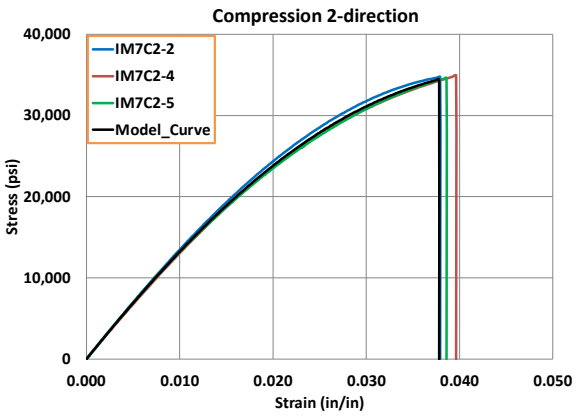

(a) (b)

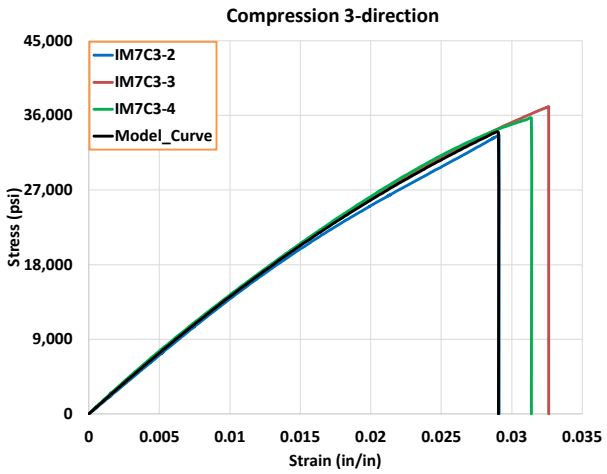

(c)

Figure 3.2. Stress-Strain from Compression Test, (a) 1- direction, (b) 2-direction, and (c) 3-direction.

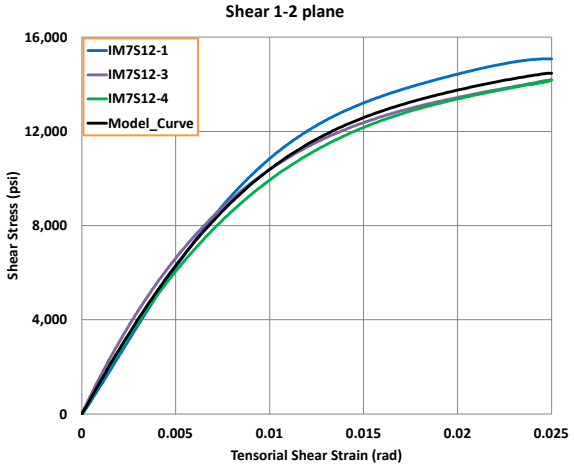

(a)

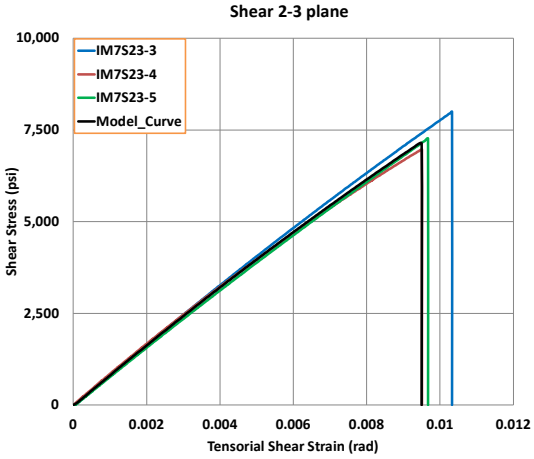

(b)

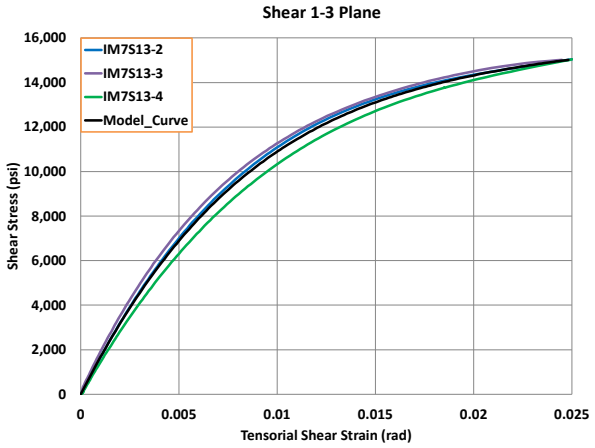

(c)

Figure 3.3. Stress-Strain curves from Shear Test, (a) 1-2 plane, (b) 2-3 plane, and (c) 1-3 plane.

3.2. CALCULATION OF ELASTIC MODULI

Elastic moduli E_a, E_b, E_c, G_{ab}, G_{bc}, and G_{ca} are the required input in cards 1 and 2 of MAT_213. E_a, E_b, E_c is taken as the slope of the initial portion of the stress-strain curve from either compression and tension tests in principal material directions a, b and c respectively. Similarly G_{ab}, G_{bc}, and G_{ca} can be calculated as the slope of the linear portion of shear stress-tensorial strain curves in principal material planes a-b, b-c and c-a respectively. In Figure. 3.5, principal material directions and planes for a unidirectional composite laminate are depicted. Figure. 3.6 shows an illustrative example to calculate E_b using stress-strain model curve from compression test in 2-direction. Table 3.2 shows the summary of Young's moduli computed using the outlined procedure.

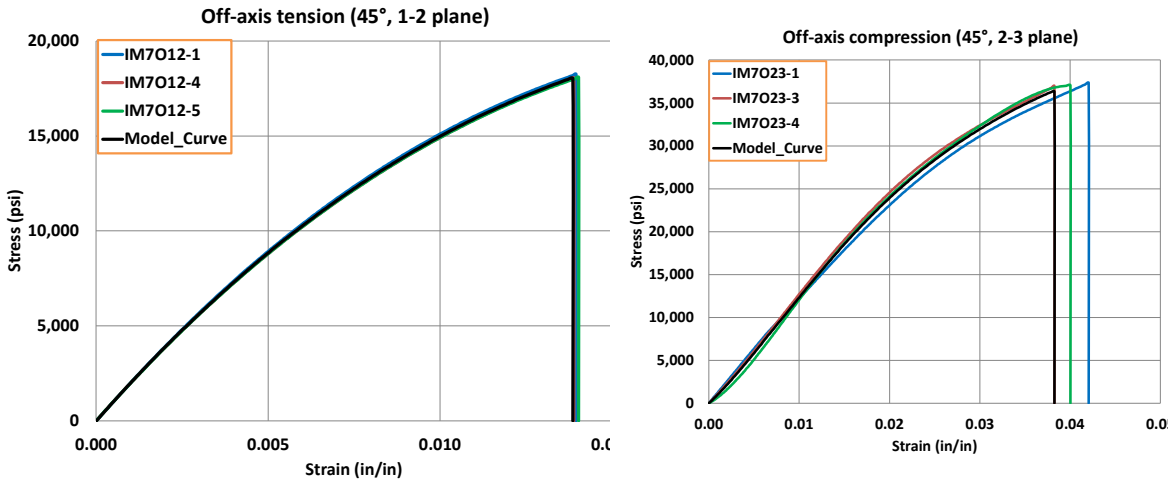

(a) (b)

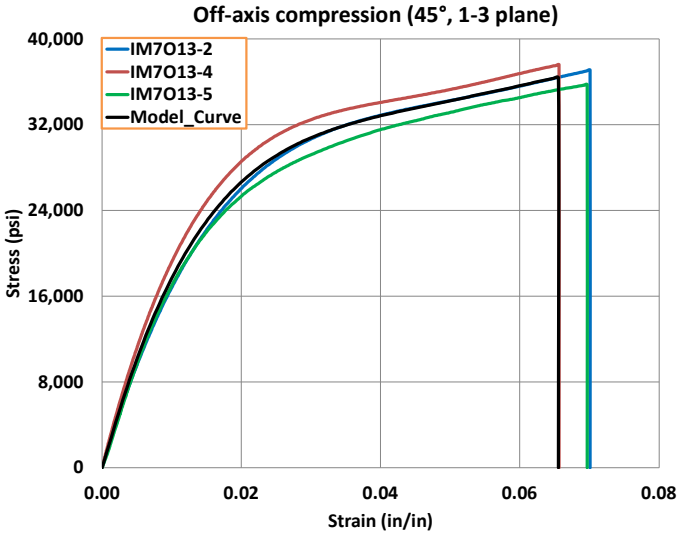

(c)

Figure 3.4. Stress-Strain Curves from Off-axis Test, (a) 1-2 plane, (b) 2-3 plane, and (c) 1-3 plane

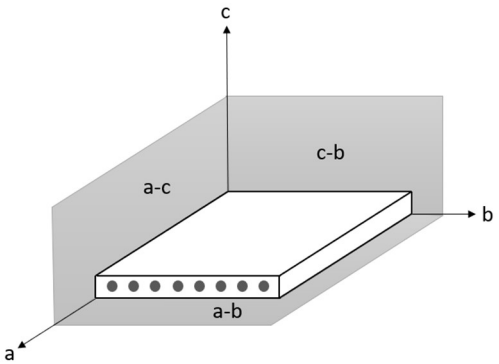

Figure 3.5. Single Ply of Unidirectional Composite Laminate Showing Principal Material

directions and planes

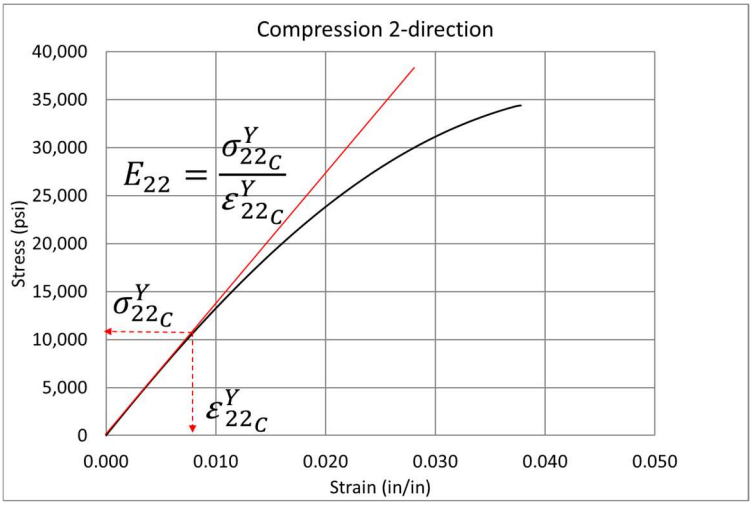

Figure 3.6. Single ply of Unidirectional Composite Laminate Showing Principal Material Directions and Planes

Table 3. Summary of Young's Moduli for IM7-8552 Composite

Young Modulus	psi
E_a	2.260e7
E_b	1.299e6
E_c	1.299e6
G_{ab}	6.22e5
G_{bc}	4.14e5
G_{ca}	6.22e5

3.3. CALCULATION OF ELASTIC AND PLASTIC POISSON'S RATIOS

The elastic Poisson's ratios are the primary inputs in MAT_213 card 1 and are obtained from the stress-strain data generated by uniaxial tension and compression tests. While the plastic Poisson's ratios are not directly utilized in MAT_213, they are used to determine the flow rule coefficients $\left(H_{11}, H_{22}, H_{33}, H_{12}, H_{23}, H_{13}, H_{44}, H_{55}, H_{66}\right)$ featured in cards 5 and 6 of the input deck.

To demonstrate the computation of the elastic and plastic Poisson's ratios in the 3-2 plane, a tension test data in the 2-3 plane is considered. To compute the elastic Poisson's ratio, the initial step involves identifying the yield strain value from the stress-total strain data, as illustrated in Figure. 3.7. This is achieved by drawing a straight-line tangent to the initial linear portion of the stress-total strain curve. The yield strain value is then determined by identifying the point where the linear portion of the curve terminates.

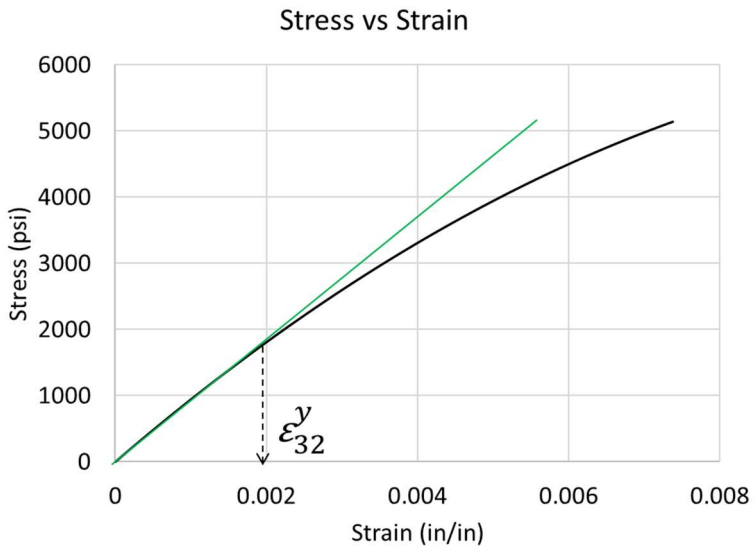

Figure 3.7. Example of Obtaining Yield Strain

Prior to the yield strain, all longitudinal and transverse strains are entirely elastic. To compute the elastic Poisson's ratio, a regression line is constructed using the longitudinal strain and negative transverse strain data before the yield strain. The slope of this regression line represents the elastic Poisson's ratio. Figure. 3.8 illustrates the calculation of ν_{32}.

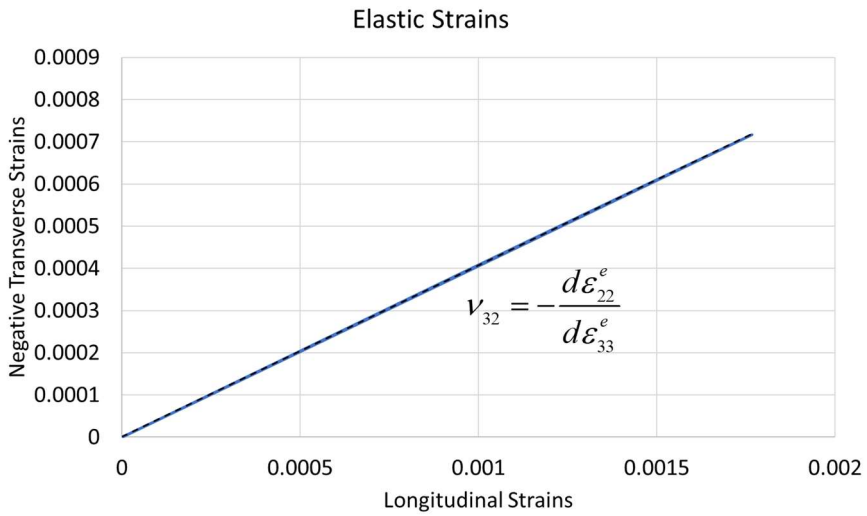

Figure. 3.8. Example of Calculating Elastic Poisson's Ratio from Tension Test Data

To compute the plastic Poisson's ratio, longitudinal and transverse plastic strains are calculated for all stress values after the yield strain, using Eq. 3.1 and Eq. 3.2, respectively. In these equations, the superscript t denotes the total strain after the yield strain, while the superscript y refers to the yield strain.

$$Longitudinal: \varepsilon_{33}^{P} = \varepsilon_{33}^{t} - \varepsilon_{33}^{y} \quad (3.1)$$

$$Transverse: \varepsilon_{22}^{P} = \varepsilon_{22}^{t} - \varepsilon_{22}^{y} \quad (3.2)$$

Finally, plastic Poisson's ratio ν_{32}^{P} is calculated by taking the slope of the regression line through longitudinal strain and transverse plastic strain data. Even though the slope of the regression line changes, an average value of 0.361 was considered. Figure. 3.9 illustrated the computation of ν_{32}^{P}.

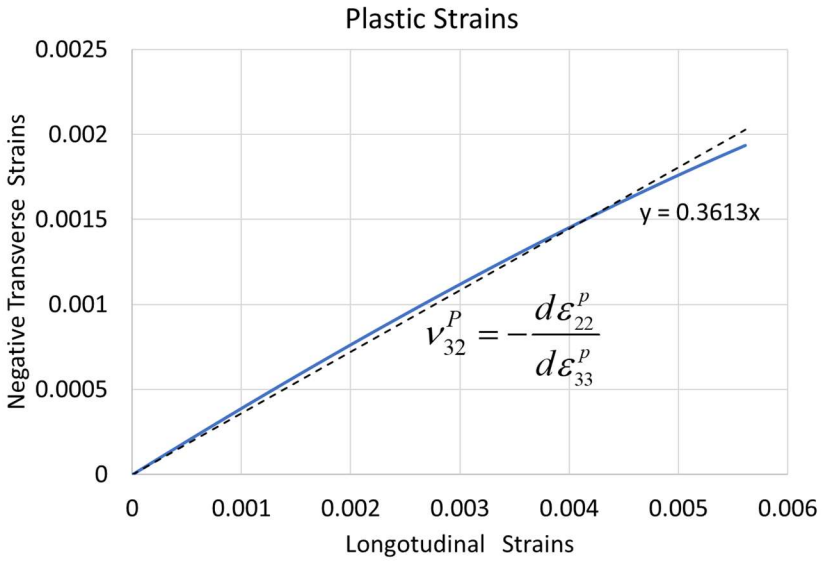

Figure 3.9. Example of Calculating Plastic Poisson's Ratio from Tension Test Data

3.4. CALCULATION OF FRC'S USING MAT213FRC COMPUTER PROGRAM

Flow rule coefficients are inputs of MAT_213 cards 6 and 7. Flow rule coefficients are used to describe the generation of plastic strains in the material through a non-associated flow rule given in Eq. 2.6. Experimental data can be used to fully characterize the flow rule coefficients introduced in Section 2. This thesis outlines the procedure for determining the flow rule coefficients for a unidirectional composite, IM7-8552. In the case of a unidirectional composite, the plastic strains in the fiber directions are always zero for all stress values, as carbon fibers exhibit linear elastic behavior. Therefor H_{11}, H_{12}, H_{13} values can be set to zero. Hence, plastic potential function can be simplified as shown in the Eq. 3.3. Flow rule coefficients are related to plastic Poisson's ratios as shown in Eq. 2.9. One cannot solve Eq. 2.9 because it is rank deficient. The common solution to this problem is assuming one of the coefficients values. The value of H_{22} is often assumed. This assumption leads to 2 direction tension or compression stress plastic

strain response being the representative effective stress-effective plastic strain $(h-\lambda)$ response of the material.

$$h^2 = H_{22}\sigma_{22}^2 + H_{33}\sigma_{33}^2 + 2H_{23}\sigma_{22}\sigma_{33} + H_{44}\sigma_{12}^2 + H_{55}\sigma_{23}^2 + H_{66}\sigma_{13}^2 \tag{3.3}$$

IM7-8552 composite exhibit isotropy in 2-3 plane and hence Eq. 3.3 can be further simplified as shown in Eq. (3.4).

$$h^2 = H_{22}(\sigma_{22}^2 + \sigma_{33}^2) + 2H_{23}\sigma_{22}\sigma_{33} + H_{44}(\sigma_{12}^2 + \sigma_{13}^2) + H_{55}\sigma_{23}^2 \tag{3.4}$$

Under plane stress condition in 1-2 plane, Eq. 3.5 can be expressed as

$$h^2 = H_{22}\sigma_{22}^2 + H_{44}\sigma_{12}^2 \tag{3.5}$$

The results from 1-2 plane tension or compression test can be used to determine the values of H_{22} and H_{44}. In this procedure 2-direction compression curve is chosen as the master curve because compression tests performed on composites provide better insight into the plasticity of the material since the ultimate failure happens well after yielding. In order to calculate H_{44}, Shear test in 1-2 plane is taken as the fitting curve.

The first step in deriving the values of H_{22} and H_{44}, is converting both master and fitting curve from stress-total strain into stress – plastic strain using Eq. 3.4. Figure. 3.11 (a) shows the resulting curves.

$$\varepsilon_{xx}^{p} = \varepsilon_{xx}^{total} - \varepsilon_{xx}^{y} \tag{3.6}$$

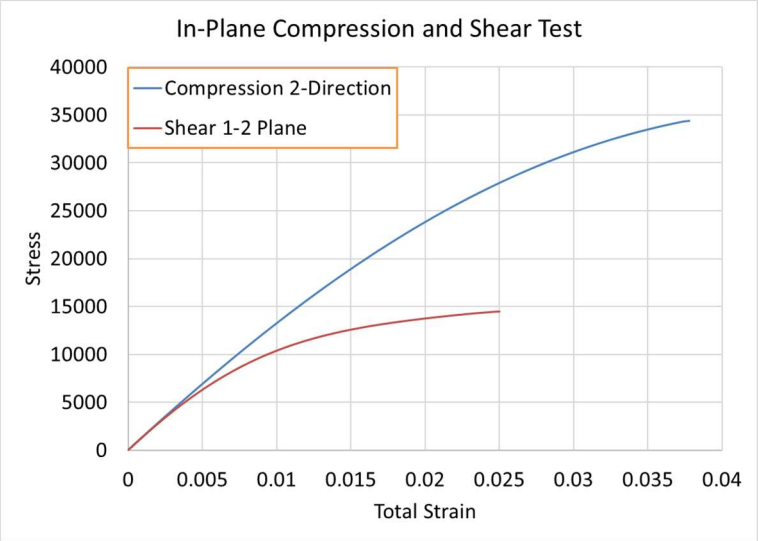

Figure 3.10. Compilation of In-plane Compression -2 direction and Shear in 1-2 plane Stress-Total Strain curves

With the assumption that effective stress-effective plastic strain is analogous to a composite property, the optimal values of H_{22} and H_{44} will result in the fitting curves collapsing onto a single unique curve in the effective stress – effective plastic strain space $(h-\lambda)$. Since there are only two degrees of freedom in Eq. 3.5, an optimization problem can be solved to find the optimal values for H_{22} and H_{44} with the only constraint being $H_{ii} \geq 0$. Using the user combination of H_{22} and H_{44}, each fitting curve is converted into $(h-\lambda)$ space using Eq. (3.3) and Eq. (3.7) respectively. Now, from the resulting fitting curves average response $(\bar{h}-\lambda)$ is computed using Eq. (3.9). Where N is the number of fitting curves.

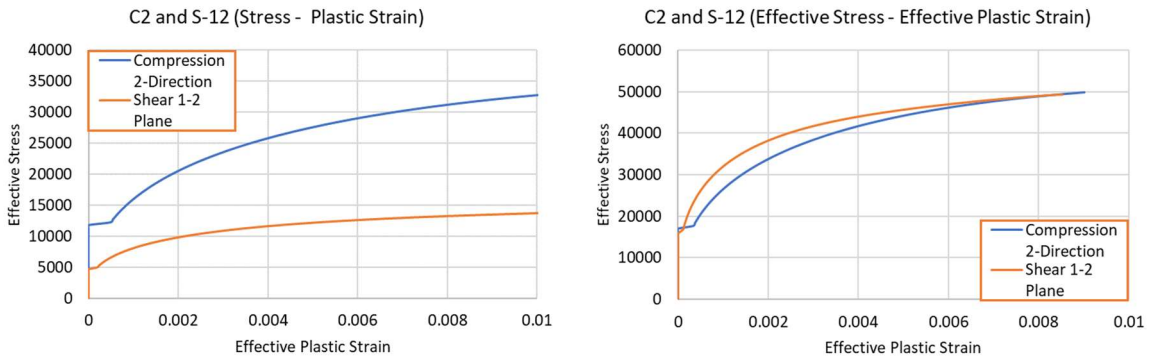

(a) (b)

Figure 3.11. (a)Compilation of In-Plane Compression -2 Direction and Shear in 1-2 Plane Curves: (a) Stress-Plastic Strain (b) Effective Stress-Effective Plastic Strain

$$\lambda = \varepsilon_e^p = \int \frac{\sigma d\varepsilon^p}{h} \tag{3.7}$$

$$\bar{h}_j = \frac{1}{N}\sum_{i=1}^{N} h_i\left(\lambda_j\right) \tag{3.8}$$

To determine how far the current combinations of H_{22} and H_{44} are from optimal, the normalized root mean square error (NRMSE) is computed between the fitting curves and the average response as

$$NRMSE = \frac{\sqrt{\frac{1}{N}\sum_{j=1}^{M_i}\sum_{i=1}^{N}\left[h_i\left(\lambda_j\right) - \bar{h}\left(\lambda_j\right)\right]^2}}{\bar{h}_{\max} - \bar{h}_{\min}} \tag{3.9}$$

Where, M_i is the number of points considered along the curves where the computation is performed. The combination of H_{22} and H_{44} which minimizes the NRMSE is considered as the optimal solution. Figure. 3.11 (b) shows the fitting curves in $(h-\lambda)$ space for a optimal combination of H_{22} and H_{44}. $H_{22} = 2.10526$ and $H_{44} = 11.5789$ were the optimal combination with a NRMSE of 0.000925993.

After computing H_{22} and H_{44}, H_{23} can be computed by using Eq. (3.8). Where, ν_{32}^{p} is the plastic Poisson's ratio that was computed in the previous section.

$$H_{23} = -\nu_{32}^{p} H_{22} \tag{3.10}$$

The remaining flow rule coefficients H_{55} and H_{66} can be computed by taking the compression in 2-direction curve as master curve and the results from shear 2-3 plane and shear 1-3 plane as fitting curves respectively. Figures. 3.12 (a) and 3.14 (b) depict the compilation of stress-plastic strain curves for 2-direction compression, with shear in the 2-3 plane and shear in the 1-3 plane, respectively. Finally, an optimization problem is solved to find optimal H_{44} and H_{55} by keeping H_{22} constant from previous step such that the curves shown in Figures. 3.13 (a) and 3.14 (a) merge into a single curve. Figure. 3.15 (b) and 3.16 (b) show the fitted curves. The optimal H_{44} and H_{55} found are 8.27586 and 11.0526 respectively. All the optimal flow rule coefficient values are presented in Table 4.

The outlined procedure to compute the flow rule coefficients was performed using a C++ written object oriented computer program called MAT213FRC [27]. Figure. 3.13 shows the flowchart of the computer program. MAT213FRC, can be used to compute all 9 flow rule coefficients for a given set of experimental data using the procedure outlined before. The program requires two input files to run and generates two output files. The first input file contains the twelve experimental stress-strain that must be formatted using specific keywords. The second input file contains details of the experimental data as well as the fitting parameters and must be formatted. Figure. 3.14 shows the formatted contents from the first and second input file for this example.

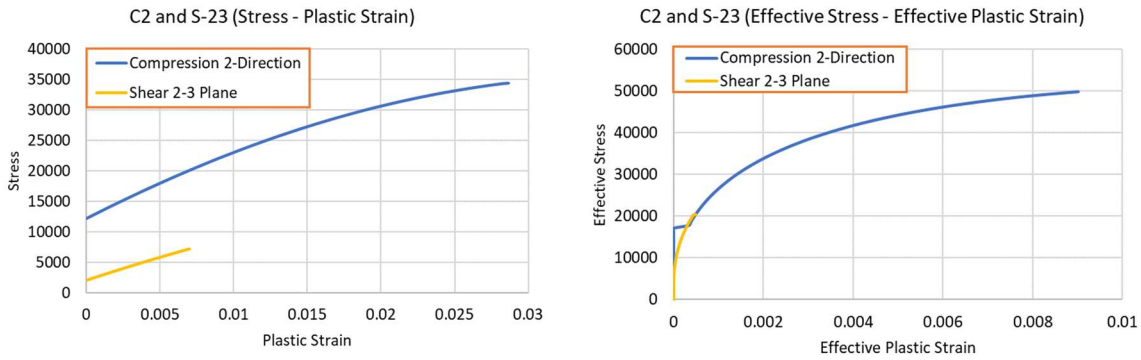

(a) (b)

Figure 3.12 (a) Compilation of In-Plane Compression -2 Direction and Shear in 2-3 Plane Curves: (a) Stress-Plastic Strain (b) Effective Stress-Effective Plastic Strain

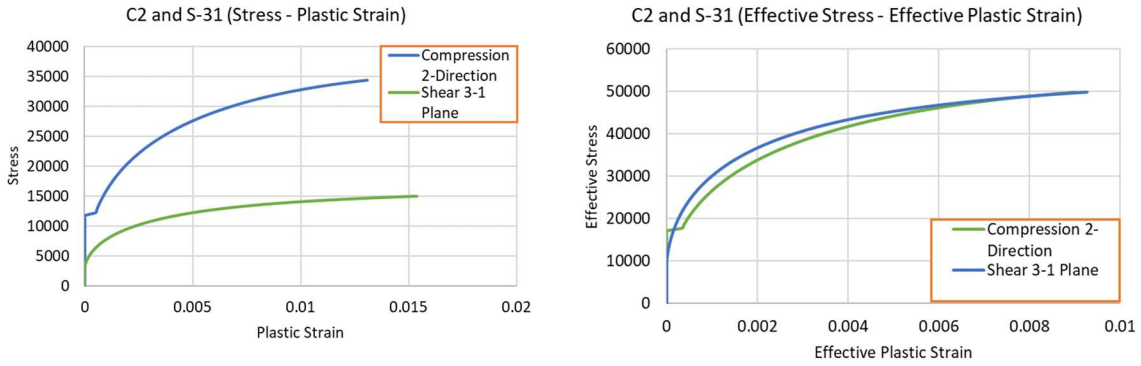

(a) (b)

Figure 3.13 (a) Compilation of In-Plane Compression -2 Direction and Shear in 3-1 Plane Curves: (a) Stress-Plastic Strain (b) Effective Stress-Effective Plastic Strain

Table 4. Optimal Flow Rule Coefficients Values for IM7-8552 Composite

Coefficient	**Optimal Value**
H_{11}	0.00
H_{22}	2.105
H_{33}	1.00
H_{44}	11.578
H_{55}	8.275
H_{66}	11.052
H_{12}	0.00
H_{23}	-0.7427
H_{13}	0.00

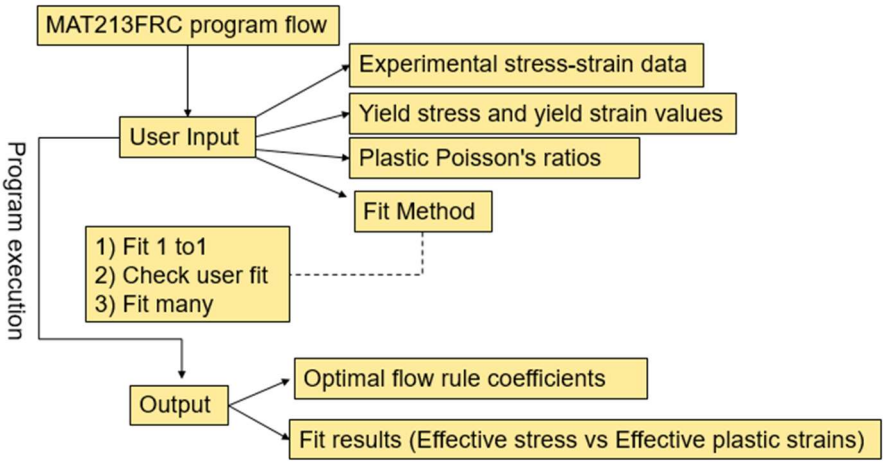

Figure 3.14. Flowchart of MAT213FRC Computer Program

```
*define_curve
1           0.0121125            294279.0
                0.0                  0.0
            0.0121125            294279.0
*define_curve
2       0.0022  2747.54
                0.0                  0.0
          0.000391435              504.776
          0.000978588              1263.05
..........


*define_curve
3       0.00207011 2272.39
           0.00000000            0.000000
          0.000069000             96.4259
          0.000138007             184.159
...........
*define_curve
4 0.0062403  113483
        0       0
0.0062403       113483
...........
```

(a)

```
*required_curves, ..\test_cases\IM7-8552\IM7-8552Data.dat
*map_curve_id
1 T1
2 T2
3 T3
4 C1
5 C2
6 C3
7 S12
8 S23
9 S31
10 O12
11 O23
12 O31
*plastic_poisson's_ratios
** nu12p, nu21p, nu23p, nu32p, nu13p, nu31p
0.00 0.00000 0.36100 0.36100 0.000000 0.000000
**********
** PART 2A
**********
***fit1to1
***shear_h_values_bounds
**H44, 0.0, 20.0
**H55, 0.0, 20.0
**H66, 0.0, 20.0
```

(b)

Figure 3.15. (a) Format of 2nd Input File (b) Format of 1st Input File

MAT213FRC provides three methods for computing flow rule coefficients. The first method, called "fit 1 to 1," uses each of the six principal normal direction curves (i.e., 1-direction tension, 2-direction tension, 3-direction tension, 1-direction compression, 2-

direction compression, and 3-direction compression) as the master curves to independently generate six different sets of flow rule coefficients. The slave curves include three off-axis curves (i.e., 1-2 plane off-axis, 2-3 plane off-axis, and 1-3 plane off-axis) and three shear curves (i.e., 1-2 plane shear, 2-3 plane shear, and 1-3 plane shear). This method is useful when the user wants to generate flow rule coefficients independently for each principal stress direction.

The second method in MAT213FRC is referred to as "Check user fit," which allows the user to evaluate the quality of the fit by selecting desired values for the flow rule coefficients and choosing any master and slave curve. This method provides an output that includes the NRMSE value for the selected fitting curves and the percentage of the original fitting curves used. This method is useful when the user wants to check the fitting quality of a specific set of flow rule coefficients.

The third method in MAT213FRC, known as "fit many," was employed in the current study. This method enables the user to select desired fitting curves and specify lower and upper bounds for all nine flow rule coefficients, which serve as the search domain for these coefficients. The output of this method includes the optimal flow rule coefficients from the best fit, NRMSE values for the fitting curves, and the percentage and number of points used in the original curves. This method is particularly useful when the user wants to obtain flow rule coefficients by fitting many curves simultaneously.

(FitMany Option) Final Flow-Rule Coefficients Table

FRC	LB	Coef	UB	Inc
H11	0	0	5	30
H22	0	2.10526	5	30
H33	0	0	0	0
H12	0	0	0	0
H23	0	0	15	30
H13	0	0	0	15
H44	0	11.5789	20	20
H55	0	0	20	30
H66	0	0	20	30

(a)

Effective Stress vs Effective Plastic Strain Curve Data

Curve	# points	Max. Effective Plastic Strain	Max. Effective Stress
C2	75	0.00901458	49804.5
S12	85	0.00852458	49249.5

Curves to Fit

Curve	Name	% of Orig. Curve Used
1	C2	22.6297
2	S12	33.873

Computed NRMSE 0.000925132

(b)

Figure 3.16. Outputs from (a) Fit-Many Option, (b) Check-User Fit Option

3.5. SINGLE ELEMENT VERIFICATION STUDY

Single element study was used to verify compatibility of the generated inputs in the previous sections with MAT_213. In Single elements verification is an important step that is undertaken before attempting more complex finite element models. The verification is done using IM7-8552 unidirectional composite experimental stress-strain curves discussed section 3.1. OEPDMM sub models (deformation, damage sub-models) were activated. Verification was done for In-plane stress-strain input curves that include tension in both 1 and 2 directions, compression in both 1 and 2 directions and shear in 1-2 plane.

Finite element modeling: All single element finite element models were constructed using 4-noded plane stress shell elements. The boundary conditions and the applied displacement are chosen such that the simulated stress and strain from the model resemble the corresponding input curve. Figure. 3.17 shows the applied boundary conditions and displacements for each of the single element shell models. The primary material directions are marked with the element with the fiber direction represented by a green line. Pin and roller supports are represented by a slashed triangle and slashed

triangle with circles respectively. Black arrows represent the direction of applied displacement.

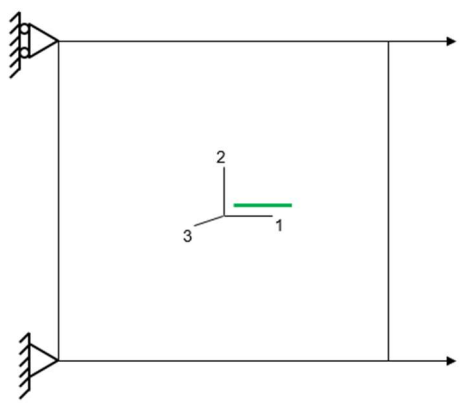

1-direction Tension

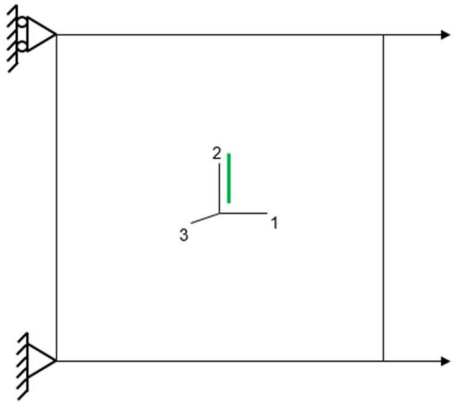

2-direction Tension

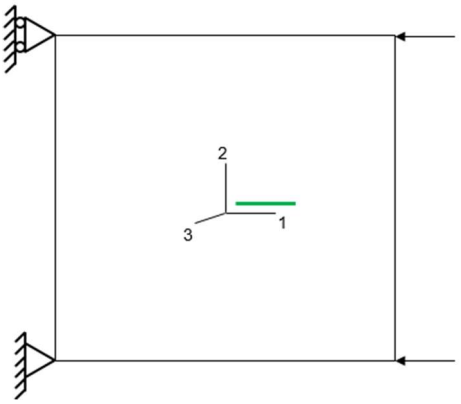

1-direction Compression

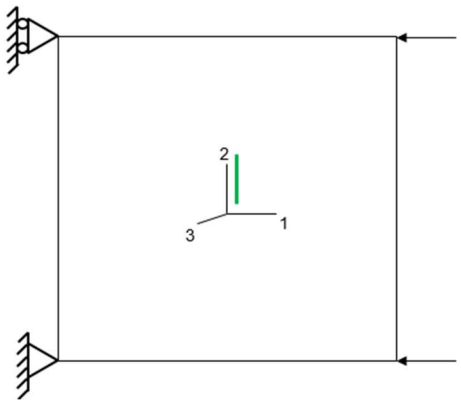

1-direction Compression

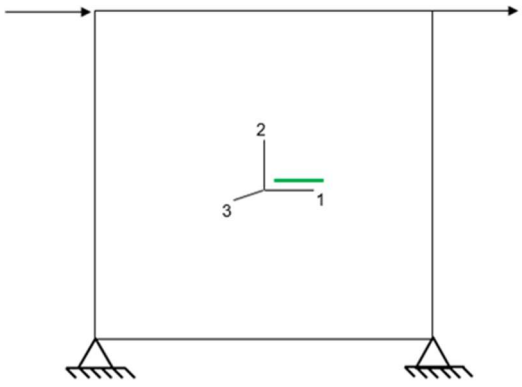

1-2 Plane Shear

Figure 3.17 Single Element Model Illustrations

Finite Element Results: Preliminary deformation only tension 1-direction model results did not agree with the model curves. This was due to the Rayleigh damping value in keyword *DAMPING_PART_STIFFNESS was set to 0.15. Similar observation was made in [28] and the correct results were obtained when a damping value of 0.05 was used. All single element models showed good agreement with the input stress-strain model curves except Shear in 1-2 plane. The configuration of boundary conditions and applied displacement shown in 'Shear 1-2 Plane (1)' in Figure. 3.17 did not induce a pure state of stress. Therefore, the results shown in Figure. 3.18 did not match the model curve. Correct results were obtained when biaxial loading configuration shown as 'Shear 1-2 Plane (2) in Figure. 3.17 was used. The single element results from all in-plane models are shown in Figure. 3.19. The MAT_213 simulation curves are represented in orange and the model curves are represented in black. The obtained results closely match the model curves. Therefore, the compatibility of IM7-8552 composite input curves with the MAT_213 is verified.

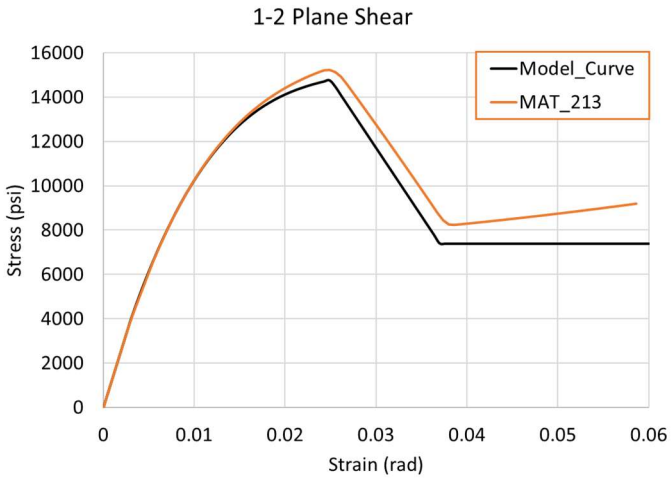

Figure 3.18. Comparison of Shear 1-2 Plane Stress-Strain Curve with MAT_213 Simulation

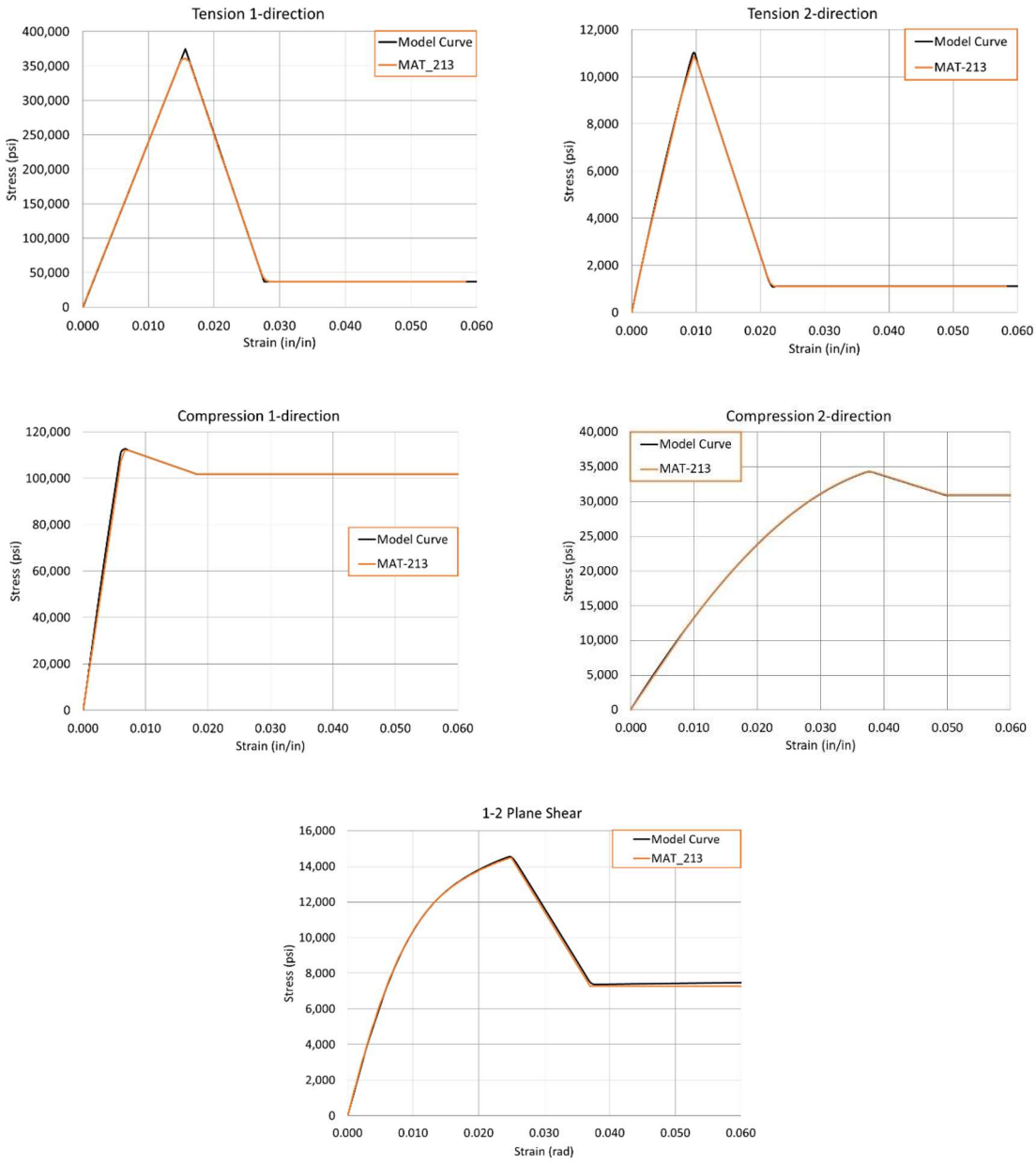

Figure 3.19 Comparison of Stress-Strain Model Curves with the MAT_213 Stress-Strain Curves

4. CHARACTERIZATION OF TRACTION SEPERATION LAW PARAMETERS FOR IM7-8552 COMPOSITE & RESPONSE SURFACE METHODOLOGY.

4.1. DCB AND ENF COUPON TESTS

ASTM D5528 [23] and D7905 [24] were followed for specimen geometries and test procedures for DCB and ENF test, respectively. A schematic diagram of DCB and ENF specimens are shown in Figure. 4.1 and Figure. 4.2. To induce mode I loading in DCB specimens, piano hinges were bonded at the end of the specimens using 3M-DP420 two-part toughened epoxy and held by spring loaded fixture on MTS exceed test frame. To induce mode II loading in ENF specimens, a standard three-point bend fixture on MTS exceed test frame was used. Both DCB and ENF experiments were performed on MTS exceed test frame using displacement rates at quasi-static condition 0.05 in/min and 0.025 in/min respectively. The test frame load cell was used to measure the forces exerted during the experiments. The displacement fields of the specimens, including the region near to the crack tip, were monitored using two-dimensional digital image correlation (2D-DIC).

A pre-cracking procedure recommended by ASTM standard was followed for both DCB and ENF in order to minimize the variation among the manufactured crack tip of different specimens. In order to conduct pre-crack cycle on DCB specimen, the specimen was loaded in mode I until the crack tip propagate approximately 0.2 in. In a similar fashion, to conduct a pre-crack cycle the ENF specimens were loaded in Mode II until the crack point propagated roughly 0.2 in. In addition, a compliance calibration was carried out on

the ENF specimens in accordance with the ASTM standard. Figure. 4.3 and Figure. 4.4 shows the measured load-displacement curves from DCB and ENF tests respectively.

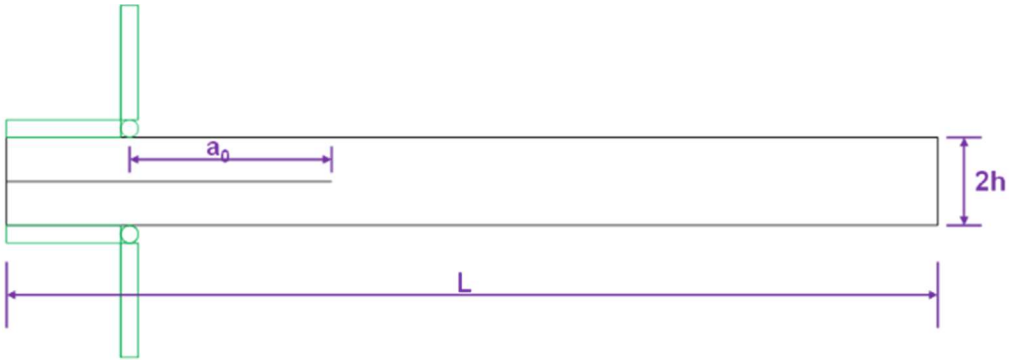

Figure 4.1. Schematic Diagram of Prepared DCB Specimen

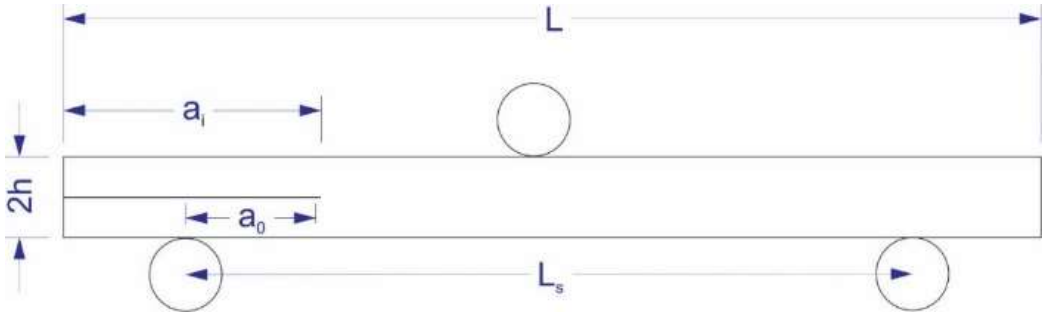

Figure 4.2. Schematic Diagram of Prepared DCB Specimen

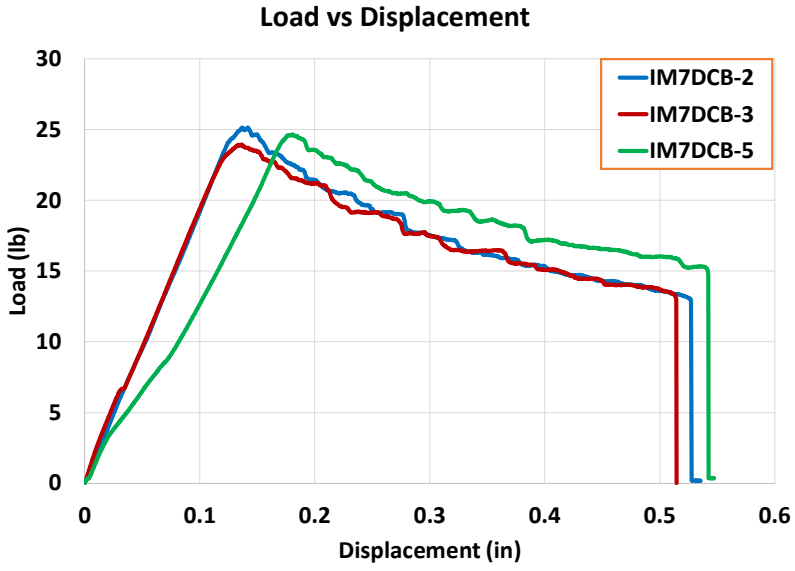

Figure 4.3. Load vs Displacement Curves: DCB

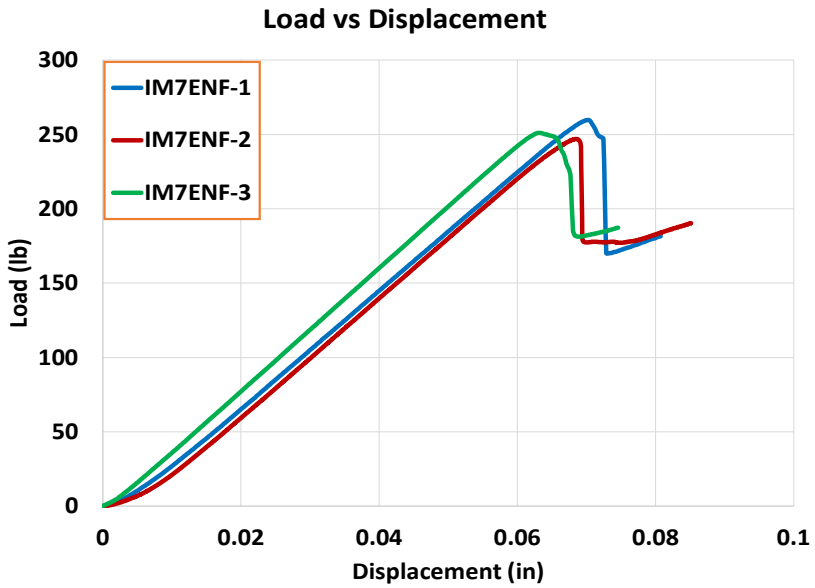

Figure 4.4. Load vs Displacement Curves: ENF

Khaled et. Al., 2019 [14] has presented a method to obtain the traction separation laws from DCB and ENF test for T800/F3900 composites by close monitoring the crack propagation during the experiment. The method requires drawing many extensometers in order to obtain crack tip opening data (CTOD) from the DIC postprocessing, which is a tedious process. There is no assurance that the CTOD values will be accurate after data is extracted from the extensometer in DIC.

In the next sections, an alternate method with response surface methodology has been presented to obtain the fracture properties for both mode 1 and mode 2 using results from DCB and ENF tests.

4.2. DCB AND ENF FINITE ELEMENT MODELS

Due to the difficulties in obtaining the fracture parameters experimentally, as briefly described in Section 4.1, it is possible to obtain both mode I and mode II fracture

parameters by performing an inverse analysis. Initially, the fracture parameters that need to be determined are obtained through a preliminary trial and error analysis to describe a cohesive zone model, which can be used in finite element analysis to capture the load displacement response from numerical DCB and ENF model. Then, the numerical load displacement curve is compared to the experimental load displacement curve determined in Section 2. The goal is to determine the optimal values of these parameters, i.e., the set of values that produces the best agreement between the numerical and experimental load–displacement curves. This is accomplished systematically by using RSM and an optimization problem described in Section 4.

Both DCB and ENF finite element models similar to those of the experiment are constructed and analyzed in LS-DYNA, a nonlinear transient dynamic finite element code, for inverse analysis. Based on the convergence and boundary condition analysis performed by Khaled et al [7], an element size of 2.54 mm (0.1 in) with an aspect ratio of 1 was chosen for both the DCB and ENF models. The composite components were modeled using MAT_213, an orthotropic plasticity material model available in LS-DYNA. MAT_213's input consists of experimentally determined material properties, which include 12 tabulated stress-strain curves corresponding to quasi-static and room temperature conditions, as well as point-wise properties such as mass density and Poisson's ratios in the 1-2, 2-3, and 1-3 planes, respectively. The input data for MAT_213 is obtained from Maurya et al. 2023 [15]. Material model MAT_186 available in LS-DYNA is used to model a single layer of cohesive zone elements extending from the initial crack tip to the end of the specimen. The primary input parameters for MAT_186 are mode I and mode II fracture properties that derive a constitutive law to determine the

relationship between stresses and relative displacements at integration points of cohesive elements. The mode I and mode II fracture properties include fracture toughness (G_{IC} and G_{IIC}), peak traction ($\sigma_{max,\ I}$ and $\sigma_{max,\ II}$), and the normalized arbitrary-shaped traction separation law (TSLI and TSLII) as shown in Figure. 4.5. Lower indices "I" and "II" indicate modes I and II, respectively, while a lower indices "c" indicates the critical value. In all simulations, the ratios of kinetic energy, sliding energy, and internal energy were examined. The ratios of kinetic and sliding energy with respect to total energy were significantly lower than the ratio of internal energy. Thus, quasi-static behavior was accurately captured.

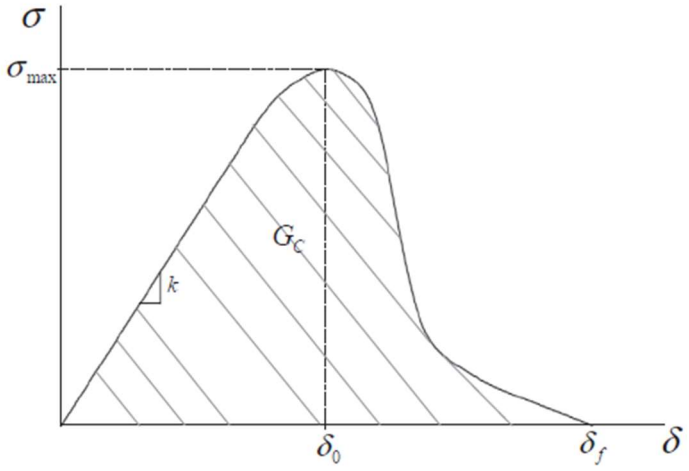

Figure 4.5. General Traction Separation Law Curve Used in MAT-186

In the DCB FE model, the geometry as depicted in Figure. 4.6(a) had the dimensions 5in x 0.1in x 0.17in. It has a 1.3-inch pre-crack region that extends from the specimen's edge. Except for the width, the model geometry was based on the experimental specimens tested by Maurya et al [15]. To reduce computational time, the width of the model was reduced to 10% of its original width. The Composite parts were constructed using 8 node

fully integrated hexahedral solid elements with ELFORM 2. The direction of the fibers in each element was aligned with the global X axis. A single layer of cohesive elements with a thickness of 2.54 x 10^{-4} mm (10^{-5} in) was modeled at the center, spanning from the initial crack tip to the edge of the composite specimen, as highlighted in yellow in Figure. 4.6(a). Additionally, the stainless-steel tabs were modeled with 8 node fully integrated hexahedral solid elements with ELFORM 2, standard steel properties were assigned. Nodal displacements (3 in/sec) were applied in the global y direction along a row of nodes on both the piano hinges 0.7in into the pre-crack region, which is highlighted in Figure. 4.6(b). All the nodes on the back face of the specimen as shown in Figure. 4.6(c) were constrained in translational degrees of freedom. The *DAMPING GLOBAL keyword in LS-DYNA was used to apply damping with a damping constant of 638.5. This value was determined based on the convergence and modal analysis performed by Khaled et al.[7].

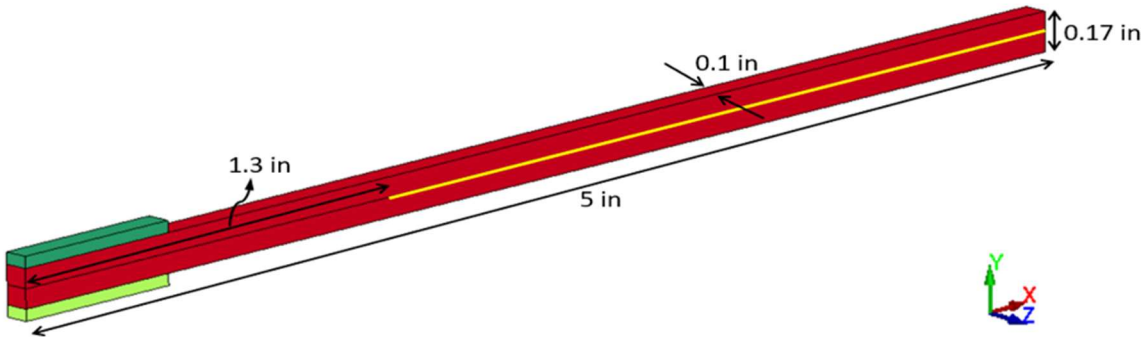

(a)

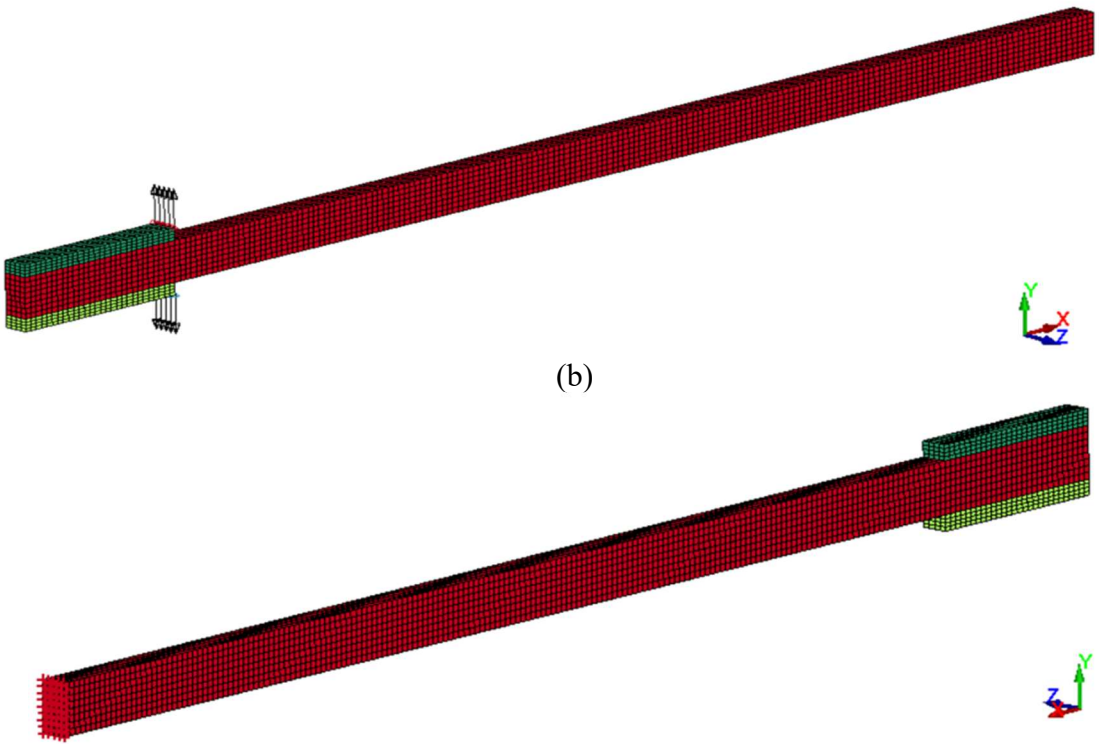

(b)

(c)

Figure 4.6. FE Model of the DCB Specimen Showing (a) Dimensions of the Specimen and the Highlighted Yellow Line Describing the Location of the Cohesive Elements, (b) Nodes on the Piano Hinges were Displacements are Applied in the Global Y direction and (c) End Face of the Specimen were All the nodes are Constrained in the Translational Degrees of Freedom.

A quadratic softening TSL, as shown in Figure. 4.7, was employed for the MAT-186 input in the DCB FE model. A nonlinear softening law was selected to account for the large-scale fiber bridging seen in Mode 1. A.B. de Morais et al. [14] demonstrated that modeling mode I with a simple linear softening law was insufficient. The TSL used for DCB has two regions: an initial undamaged linear elastic region, followed by a non-linear damage region. The area under the damage region was assumed to be equal to the area of a parabolic spandrel for purposes of simplification. The complete characterization of the chosen TSL can be done by using 4 parameters, G_{IC}, $\sigma_{\max,I}$, $\delta_{o,I}$ and $\delta_{f,I}$, where G_{IC} is the

area under the TSL, $\sigma_{\max,I}$ is the peak traction in mode I, $\delta_{o,I}$ is the damage initiation crack tip opening displacement (CTOD), and $\delta_{f,I}$ is the failure CTOD in mode I. G_{IC}, $\sigma_{\max,I}$, $\delta_{o,I}$ are independent parameters whereas $\delta_{f,I}$ is dependent parameter and can be calculated by using Eq. 4.3. Independent parameters are used in the RSM as design variable in section 4 to obtain optimal parameter values. G_{IC} was used as a design variable in RSM even though the value was obtained experimentally to account for the inaccuracies due to linear elastic assumptions in the compliance method and various other experimental aspects such as crack tip rotations, shear deformations, and small-scale yielding to achieve a better G_{IC}.

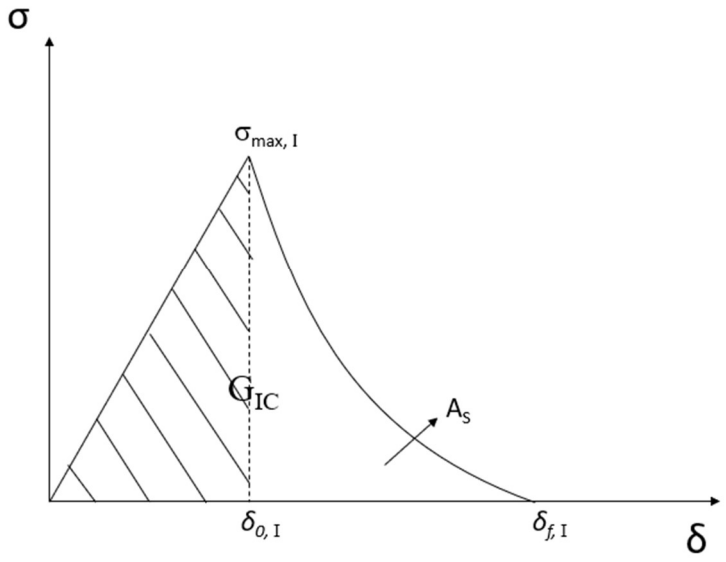

Figure 4.7. The Mode I Traction Separation Law

From Figure. 4.7, the area of parabolic spandrel (unhatched region) can be written as

$$A_s = G_{IC} - \frac{1}{2}\sigma_{\max,I}\left(\delta_{o,I}\right) \tag{4.1}$$

Also, from Figure. 4.7

$$A_s = \frac{1}{3}\left(\delta_{f,I} - \delta_{o,I}\right)\sigma_{\max,I} \tag{4.2}$$

Substituting area obtained from Eq. 4.1 in Eq. 4.2 we get

$$\delta_{f,I} = \frac{3A_s}{\sigma_{\max,I}} + \delta_{o,I} \tag{4.3}$$

To generate data for RSM, lower and upper bounds must be specified for each of the three design variables. The bounds represent the boundary value of the design variables, which were determined through a preliminary analysis based on trial and error. The analysis involves tweaking the design variables by comparing the experimental load displacement curve to several simulation load-displacement curves. A middle bound was chosen for all design variables close to the optimal region presumed based on simulation results for boundary parameters. In Figure. 4.8, the simulation results for the boundary parameters are compared to the experimental curve whereas, Table 3.1 displays the bounds and corresponding design variable values. The reaction load was calculated as the sum of the nodal reaction forces across the width of the top beam. Since the specimen's width was scaled to 10% of its original width, the obtained total load was multiplied by a factor of 10. The simulation displacement was obtained by plotting the nodal displacement of the top beam's corner node in the global y-direction.

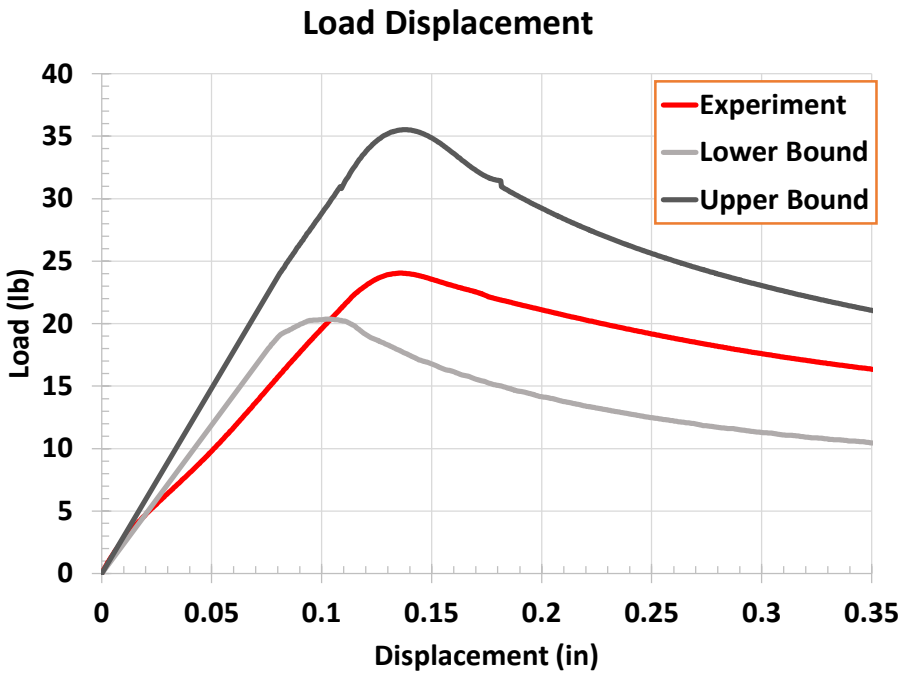

Figure 4.8. DCB Simulation Results for Boundary Parameters

Table 5. DCB Design Variable Bounds

Parameters	Bounds		
	Lower	Middle	Upper
G_{IC} (lb – in / in^2)	1.2	1.85	3
$\sigma_{\max,I}$ (lb / in^2)	300	700	1100
$\delta_{o,I}$ (in)	0.0012	0.0016	0.002

In the ENF FE model, the dimensions of the geometry are depicted in Figure. 4.9 were 6.5in x 0.5in x 0.25in. The ENF model, like the DCB model, has a 2.3-inch pre-crack region that extends from the specimen's edge. The model geometry was based on the experimental specimens tested by Maurya et al. [15], except for the width. The width of the model was reduced to 50 percent of its original width to reduce computation time. 8 nodes of fully integrated hexahedral solid elements with ELFORM 2 were used to construct the composite parts. Each element's fiber orientation was aligned with the

global X axis. As depicted in Figure. 4.9, a single layer of cohesive elements with a thickness of 2.54 x 10^{-4} mm (10-5) was modeled in the center, spanning from the initial crack tip to the edge of the composite specimen (a). The support and loading fixtures were modeled as rigid bodies using LS-DYNA's MAT_20 material model. The typical elastic properties of steel were used. The supporting fixtures were fully constrained in all translational and rotational degrees of freedom. The loading fixture was also constrained in all translational and rotational degrees of freedom except for translation in the global y direction. A prescribed global y displacement rate of 5 in/sec was applied to the loading fixture. Contacts were defined between the support fixtures or loading cell and the composite by using *CONTACT_AUTOMATIC_SURFACE_TO_SURFACE definition in LS-DYNA. Static and dynamic friction coefficients were set to 0.1, based on values used by Khaled et al. [7].

In the preliminary analysis, both linear and nonlinear softening laws were investigated for MAT_186 input in the ENF FE model. The results obtained showed little difference between the two softening laws. As depicted in Figure. 4.10, a linear softening TSL was chosen and used as an input in the MAT_186 cohesive zone model. Similar to DCB model, The TSL used for ENF model has two regions. An initial undamaged linear elastic region followed by a linear damage region. The area under the damage region is a right-angle triangle. As with DCB model, G_{IIC}, $\sigma_{\max,II}$, $\delta_{o,II}$, and $\delta_{f,II}$ can be utilized to complete the characterization of the bi-linear TSL, where G_{IIC} is the area under the TSL, $\sigma_{\max,II}$ is the peak traction in mode II, $\delta_{o,II}$ is the damage initiation CTOD, and $\delta_{f,II}$ is the failure CTOD in mode II. G_{IIC}, $\sigma_{\max,II}$, $\delta_{o,II}$ are independent parameters whereas $\delta_{f,II}$ is dependent

parameter and can be calculated by using Eq. 4.6. Like DCB test, independent parameters are used in the RSM as design variable in section 4 to obtain mode II optimal cohesive law parameter values.

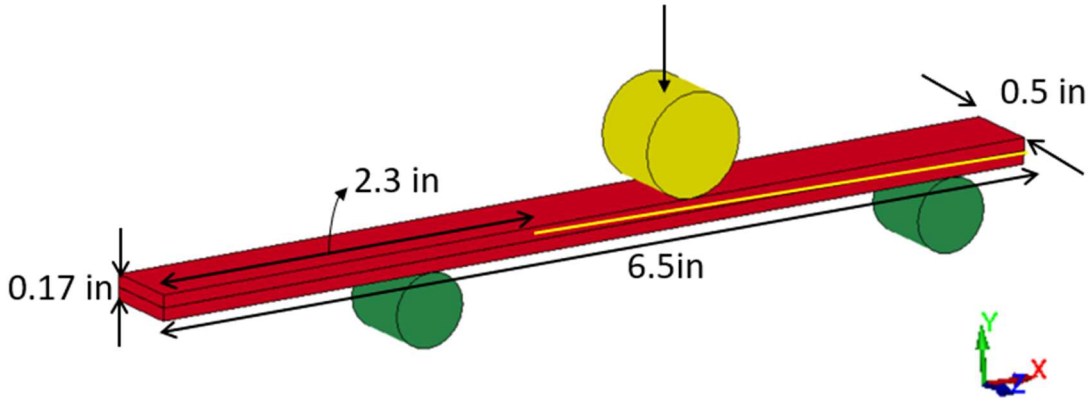

Figure 4.9. FE Model of the ENF Specimen Showing Dimensions of the Specimen and the Highlighted Yellow Line Describing the Location of the Cohesive Zone Elements.

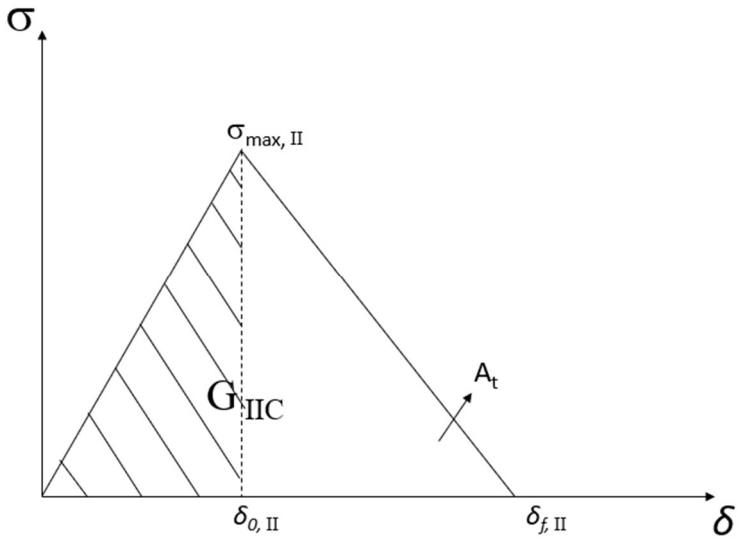

Figure 4.10. ENF Simulation Results for Boundary Parameters

From Figure. 4.10: The area of the triangle (unhatched region) can be written as

$$A_T = G_{IIC} - \frac{1}{2}\sigma_{\max,II}\left(\delta_{o,II}\right) \tag{4.4}$$

Also, from Figure. 4.10

$$A_T = \frac{1}{2}\left(\delta_{f,II} - \delta_{o,II}\right) \tag{4.5}$$

Substituting the value of A_T obtained from Eq. 4.4 in Eq. 4.5 we get

$$\delta_{f,II} = \frac{2A_T}{\sigma_{\max,II}} + \delta_{o,II} \tag{4.6}$$

Similar procedures were followed in the ENF model as in the DCB model to generate the data for RSM in Section 4. Lower, middle, and upper bounds were established by performing a trial-and-error-based preliminary analysis by comparing the experimental load displacement curve obtained in Section 2 with several simulation load displacement curves. Table 3.2 shows the bounds and the corresponding design variable values. Figure. 4.11 compares the smoothed simulation results for the boundary parameters to the smoothed experimental curve. The reaction load was extracted from the contact defined between the support fixtures and composite parts. Since the model width was scaled to 50% of the actual width, the obtained load values were multiplied by a factor of 2. Displacement results were obtained by plotting the nodal displacement of a load cell node in the global y direction.

Table 6. ENF Design Variable Bounds

Parameters	Bounds		
	Lower	Middle	Upper
G_{IIC} (lb – in / in^2)	3	5	8
$\sigma_{\max,II}$ (lb / in^2)	1500	4000	6000
$\delta_{o,II}$ (in)	0.0005	0.0015	0.0024

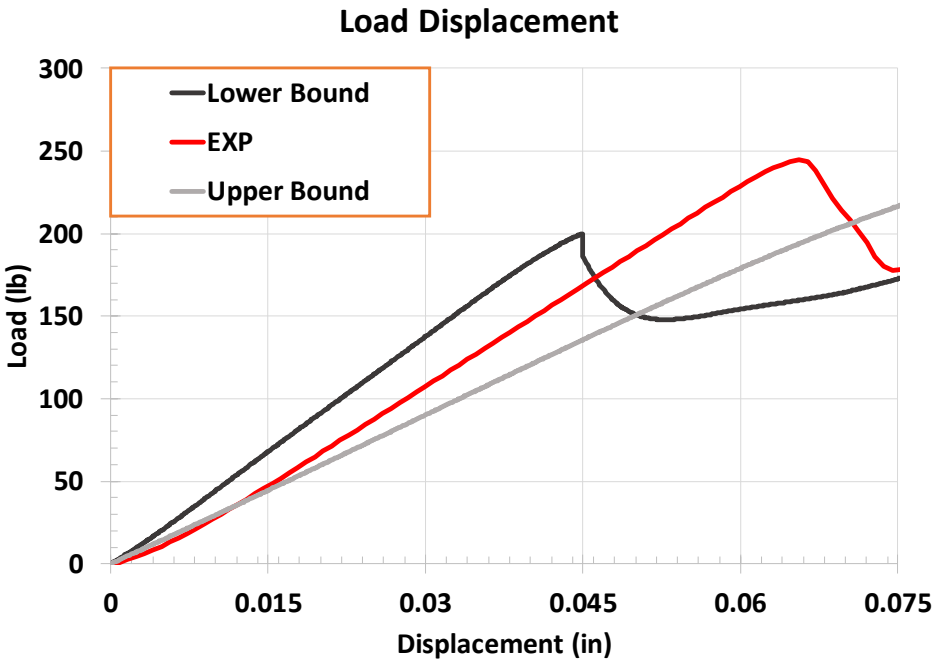

Figure 4.11. ENF Simulation Results for Boundary Parameters

4.3. RESPONSE SURFACE METHODOLOGY

Response Surface Methodology (RSM) is a mathematical and statistical technique utilized for process optimization and experiment design. It is used to evaluate the systematic relationship between a response variable and a set of predictor variables. Response variable is a quality characteristic whereas, predictor variables are parameters that affect the response variable. RSM can be effectively used to study the effect of multiple variables on a response, as well as to study the interaction between variables. RSM is also called as 3^k factorial design where, "k" is the number of predictor variables and 3^k refers to the fact that each predictor variable has three levels (lower, middle, and upper bounds).

In our current study, RSM (3^k factorial design) is utilized to obtain both mode I and mode II optimal cohesive law parameters. In our case, the independent design variables for both mode I and mode II are G_C, $\sigma_{\max}$, and δ_o. Since this is a 3^K factorial design, the lower, middle, and upper bounds (Table 3.1 and Table 3.2) for all design variables obtained from both DCB and ENF tests in section 3 were used to generate 27 data points. Each data point represents a unique combination of the three independent variables. The combinations of all the data points are shown in Table 3.3. Each unique combination of design variables in 27 data points from both modes I and II was utilized to generate a unique traction separation law curve. Then, each TSL was utilized as an input for MAT_186 in the DCB and ENF models described in section 2, and finite element analysis was performed. This corresponded to a total of 27 simulations each for the DCB and ENF tests. Using the method outlined in Section 3, the load displacement response of each simulation was extracted. The subsequent sections 4.1 and 4.2, respectively, explain how to generate the response surface and determine the optimal design variables by fitting the response surface with a polynomial for both DCB and ENF tests respectively.

Table 7. Design Variable Combination Using Low, Medium, and High bounds.

Data Point	**Combinations**		
	G_C	**σ_{max}**	**δ_o**
1	Low	Low	Low
2	Low	Low	Medium
3	Low	Low	High
4	Low	Medium	Low
5	Low	Medium	Medium
6	Low	Medium	High
7	Low	High	Low
8	Low	High	Medium

9	Low	High	High
10	Medium	Low	Low
11	Medium	Low	Medium
12	Medium	Low	High
13	Medium	Medium	Low
14	Medium	Medium	Medium
15	Medium	Medium	High
16	Medium	High	Low
17	Medium	High	Medium
18	Medium	High	High
19	High	Low	Low
20	High	Low	Medium
21	High	Low	High
22	High	Medium	Low
23	High	Medium	Medium
24	High	Medium	High
25	High	High	Low
26	High	High	Medium
27	High	High	High

4.3.1. DCB RSM

RSM comprises 3 steps. 1st step is to generate response surface / objective function. Response surface can be a quality characteristic of a system. In our study, the load difference between the experimental and simulation load-displacement curve at several values of displacements was considered as a response variable. Displacements at which the load difference are evaluated are called as sample points. Figure. 4.12 illustrates the load difference at a sample point. All 27-load displacement results from DCB were discretized into 12 sample points. 12 number of sample points were sufficient to ensure that the error calculation between the two curves is accurate. The location of the sample points was same for all the curves. At these sample points root mean squared error

(RMSE) was evaluated using Eq. 4.7. The RMSE obtained from all the 27 data points were used as the response surface / objective function.

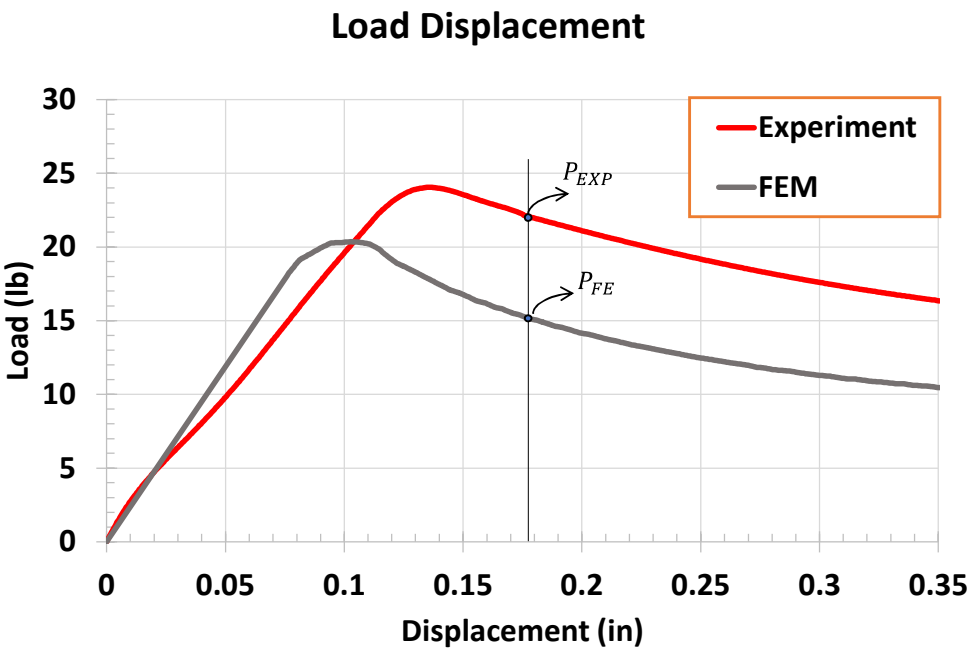

Figure 4.12. DCB Load Difference at a Sample Point

$$f(x) = \sqrt{\frac{\sum_{i=1}^{n}\left(\left(P_{FEM}\right)_i - \left(P_{EXP}\right)_i\right)^2}{n}} \tag{4.7}$$

Figure. 4.13 depicts the DCB test simulation load displacement results from all 27 data points. All the simulations and experimental curves were smoothed before calculating the error function. A good amount of scatter in the load displacement responses was observed. Table 4.1 displays the objective/error function evaluated at each data point. Data point 12 and its combination of design variables yielded the best results, while data point 25 yielded the worst.

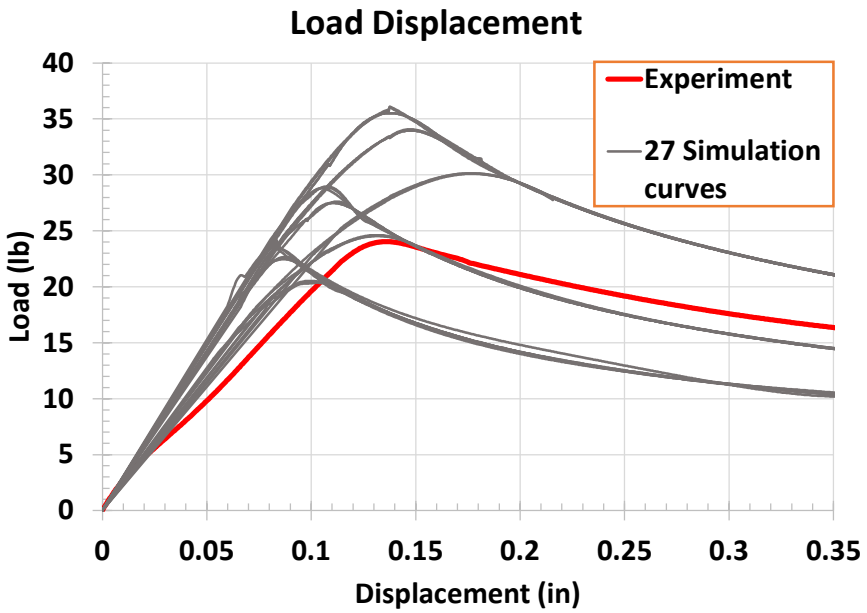

Figure 4.13. DCB 27 Simulations Results

Table 8. DCB 27 Combinations with Calculated Error Function.

Data Point	G_{IIC}	$\sigma_{max, II}$	$\delta_{o, II}$	f(x)
1	1.2	300	0.0012	5.242
2	1.2	300	0.0016	5.102
3	1.2	300	0.002	5.019
4	1.2	700	0.0012	5.610
5	1.2	700	0.0016	5.888
6	1.2	700	0.002	5.440
7	1.2	1100	0.0012	6.446
8	1.2	1100	0.0016	5.881
9	1.2	1100	0.002	5.992
10	1.85	300	0.0012	2.049
11	1.85	300	0.0016	2.213
12	1.85	300	0.002	**1.790**
13	1.85	700	0.0012	3.983
14	1.85	700	0.0016	3.422

15	1.85	700	0.002	3.411
16	1.85	1100	0.0012	4.159
17	1.85	1100	0.0016	4.547
18	1.85	1100	0.002	4.283
19	3	300	0.0012	5.465
20	3	300	0.0016	5.413
21	3	300	0.002	5.675
22	3	700	0.0012	7.414
23	3	700	0.0016	7.389
24	3	700	0.002	7.265
25	3	1100	0.0012	**8.423**
26	3	1100	0.0016	8.141
27	3	1100	0.002	8.141

After the response surface or the objective function is obtained, the next step in RSM is to fit the objective function with a second-order polynomial. This was achieved by using the Levenberg-Marquardt Algorithm (LMA), which is an optimization technique used to fit a polynomial with a set of data points. Eq. 4.8 shows the second-order polynomial considered. c_0, c_1, c_2, c_3, c_4, c_5, c_6, c_7, c_8, and c_9 are the coefficients to be determined by fitting the polynomial with the objective function whereas, variable x is G_{IC}, variable y is $\sigma_{\max,I}$ and variable z is $\delta_{o,I}$. The objective of using LMA is to find the coefficient values that minimize least-squared error between the objective function and the fitting function. Eq. 4.9 shows the least squared problem solved using LMA where, $f_i^{fit}(c)$ is the fitting function and $f_i(x)$ is the error function which is taken from Table 4.1. To conduct LMA, Eigen test library (https://eigen.tuxfamily.org/) was used, which is an open C++ library

than can be used to perform linear algebra operations including LMA. Using the C++ program, the coefficients of the fitting function were obtained, which are shown in Eq. 4.10.

$$f^{fit}(c) = c_0 + c_1 x + c_2 y + c_3 z + c_4 x^2 + c_5 y^2 + c_6 z^2 + c_7 xy + c_8 xz + c_9 yz \tag{4.8}$$

Find c to minimize,

$$\sum_{i=1}^{27} \left(f_i^{fit}(c) - f_i(x) \right)^2 \tag{4.9}$$

$$\begin{aligned} f^{fit}(c) = {} & 17.8311 - 16.06x + 0.00329y - 214.458z + 3.76x^2 - 0y^2 - 64959.8z^2 + \\ & 0.0011xy + 148.55xz - 0.176yz \end{aligned} \tag{4.10}$$

The final step in RSM is to obtain the optimal cohesive parameters (G_{IC} , $\sigma_{\max,I}$, $\delta_{o,I}$) that will result in the desired response. This is achieved my minimizing the objective function by solving an optimization problem. The obtained cohesive zone parameters were $G_{IC} = 2.0534$, $\sigma_{\max,I} = 4198.09$, and $\delta_{o,I} = 0.001935$ respectively. Traction separation law using the optimal cohesive parameters was constructed as shown Figure. 4.14, which was incorporated in cohesive zone model (MAT_186). Finite element analysis was conducted for DCB model as described in section 3. The obtained results from optimal cohesive parameters, which are compared against the best combination and the experimental model curve, are shown in Figure. 4.15. The load-displacement response from using optimal cohesive parameters is represented by the blue color, whereas the best load displacement curve from datapoint 12 combination is represented by the green color. A good agreement with the experimental results in both pre-peak and post-peak regions is observed for both curves. However, much better post-peak results are captured by the

optimal curve. The optimal curve has an RMSE value of 1.70 pounds per sample point compared to the best curve that has an RMSE value of 1.79 pounds per sample point.

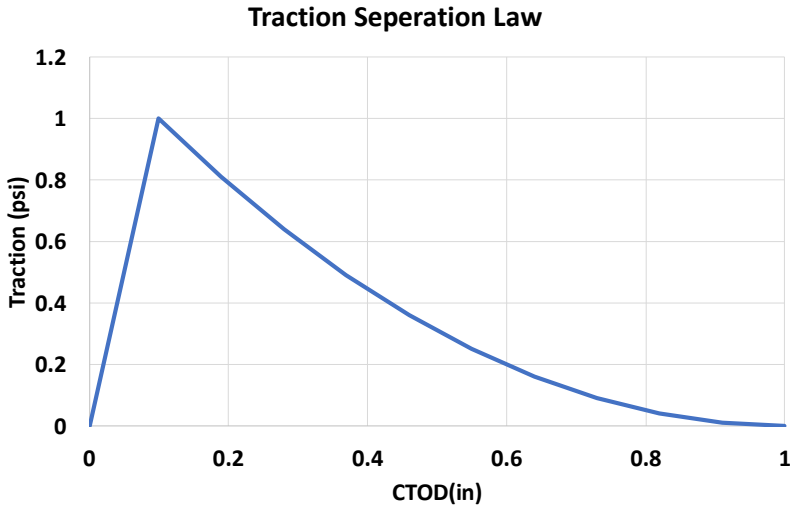

Figure 4.14. DCB Traction Separation Law Constructed Using Optimal Cohesive Zone Parameters.

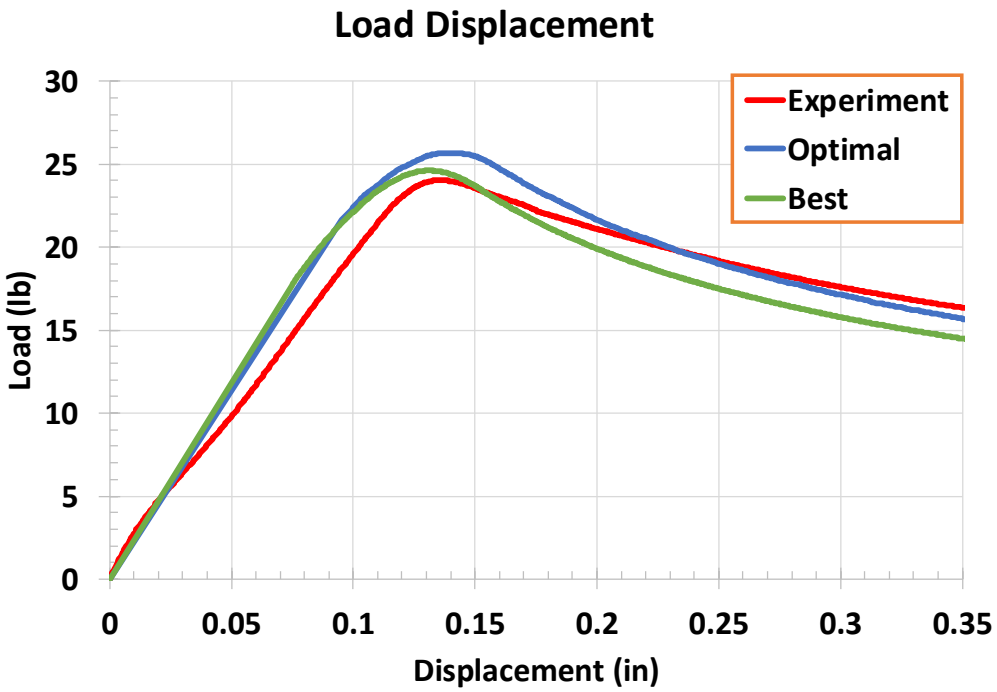

Figure 4.15. ENF Optimal Load Displacement Curve Compared with the Best and Experimental Results.

4.3.2. ENF RSM

The optimal mode II cohesive law parameters for ENF test were achieved using a similar methodology as that used for the DCB test. In order to facilitate 3k design, 27 combinations of mode II cohesive law parameters were constructed using the lower, middle, and upper bounds shown in Table 3.2. Traction separation laws were constructed for all combinations except combinations 2, 3, 6, and 12, as invalid traction separation law was observed with $\delta_{o,II}$ being greater than $\delta_{f,II}$ for these combinations. As a result, data points 2, 3, 6, and 12 were omitted from the RSM data. Using the constructed traction separation laws, 23 ENF cohesive zone finite element models were constructed and analyzed. The ENF FE model details are described in detail in section 3. The result from these simulations shows a good scatter in load displacement responses as depicted in Figure. 4.16. Like in DCB, RMSE was computed using experimental and simulation load displacement curves to generate the objective function. The load displacement curves from each data point was smoothed and was discretized into 12 sample points. Figure. 4.17 shows the load difference between the simulation and experimental load-displacement curve evaluated at a sample point for an ENF test. Eq. 7. was used to calculate the RMSE for all the 23 simulation results and is displayed in Table 4.2. Data point 15 cohesive law parameter combination was the best with a RMSE of 13.49lb at each sample point whereas, data point 19 cohesive law parameter combination was the worst with a RMSE of 60.11lb at each sample point.

After objective function is obtained, the next step is to fit the objective function with a second-order polynomial. Similar to DCB, Eq. 4.8. was taken as the fitting function and Levenberg-Marquardt Algorithm (LMA) was used to fit the polynomial with the

objective function to obtain the coefficient values. Eq. 4.9 was solved using LMA to find the coefficients shown in Eq. 4.11.

$$f^{fit}(c) = 111.164 + 31.8731x - 0.00474451y + 714.007z + 2.59859x^2 + 0y^2 + 2456720z^2 + 0xy - 156.107xz - 2.245264c_9yz \quad (4.11)$$

Finally, an optimization problem was solved in order to get the optimal mode II cohesive law parameter by minimizing Eq. 4.11. The obtained parameters were $G_{IIC} = 5.32276$, $\sigma_{\max,II} = 4198.43$ and $\delta_{o,II} = 0.00193954$ respectively. A TSL was constructed (Figure. 4.18) and used in MAT_186 input in an ENF FE model described in section 3 to run the analysis. The blue color curve in Figure. 4.19 depicts the load displacement result attained using the optimal cohesive law parameters compared against the best curve in green (from data point 15) and experimental curve in red. The optimal curve was better with an RMSE of 13.05lb per sample point compared to the best curve which has an RMSE of 13.49lb per sample point. The mode II traction separation law was constructed using the obtained cohesive law parameters and was subsequently used in a flat-plate crush simulation for validation of the mode II fracture parameters.

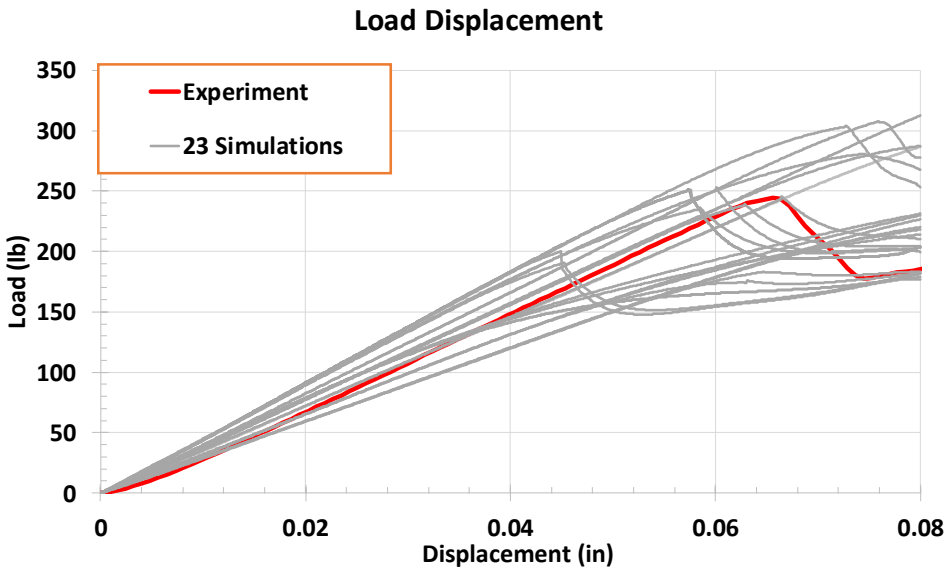

Figure 4.16. 23 ENF Simulation Results

Table 9. ENF 27 Data Point Combinations and Error Function

Data Point	G_{IIC}	$\sigma_{max, II}$	$\delta_{o, II}$	f(x)
1	3	6000	0.0005	48.56
2	3	6000	0.0015	-
3	3	6000	0.0024	-
4	3	4000	0.0005	40.96
5	3	4000	0.0015	41.18
6	3	4000	0.0024	-
7	3	1500	0.0005	40.77
8	3	1500	0.0015	35.45
9	3	1500	0.0024	29.22
10	5	6000	0.0005	29.59
11	5	6000	0.0015	20.92
12	5	6000	0.0024	-
13	5	4000	0.0005	23.71
14	5	4000	0.0015	13.79
15	5	4000	0.0024	**13.49**

16	5	1500	0.0005	26.00
17	5	1500	0.0015	27.44
18	5	1500	0.0024	31.76
19	8	6000	0.0005	**60.11**
20	8	6000	0.0015	54.47
21	8	6000	0.0024	45.12
22	8	4000	0.0005	46.51
23	8	4000	0.0015	40.89
24	8	4000	0.0024	34.66
25	8	1500	0.0005	23.70
26	8	1500	0.0015	27.23
27	8	1500	0.0024	31.99

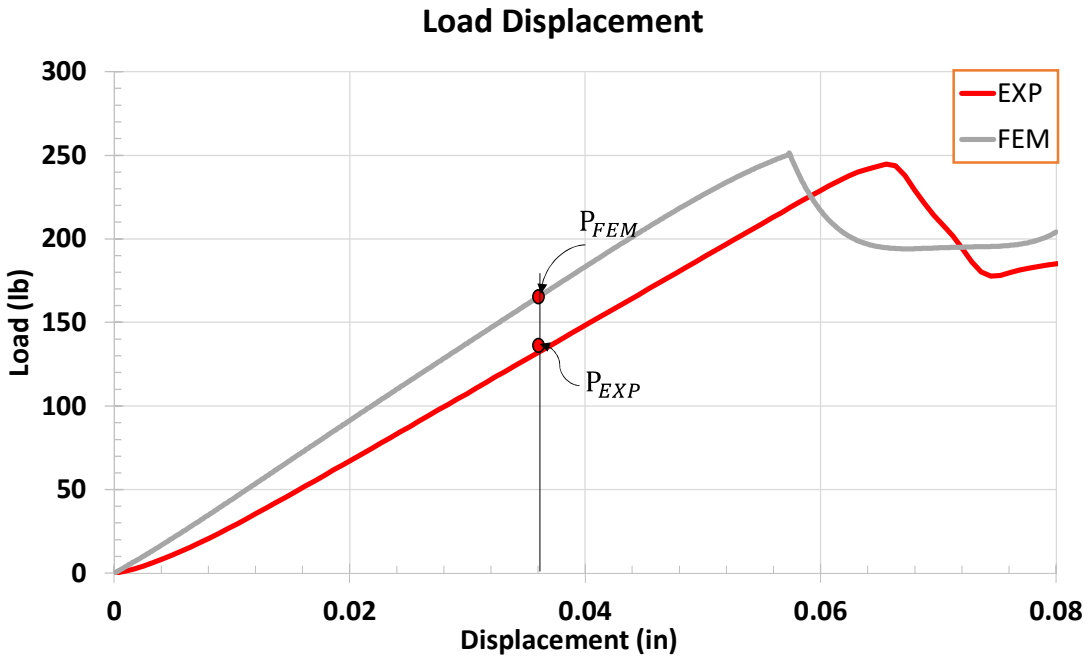

Figure 4.17. ENF Load difference at a Sample Point

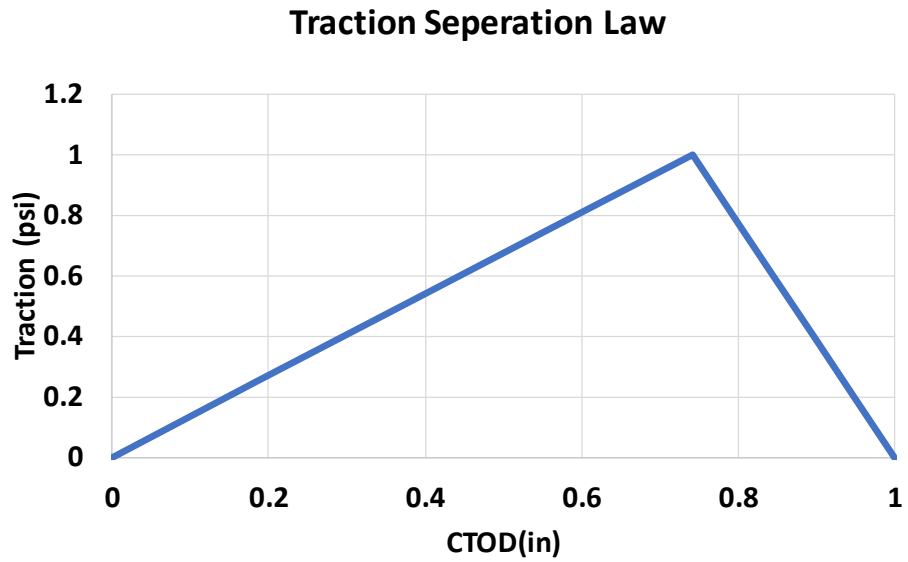

Figure 4.18. ENF Traction Separation Law Constructed Using Optimal Cohesive Zone Parameters.

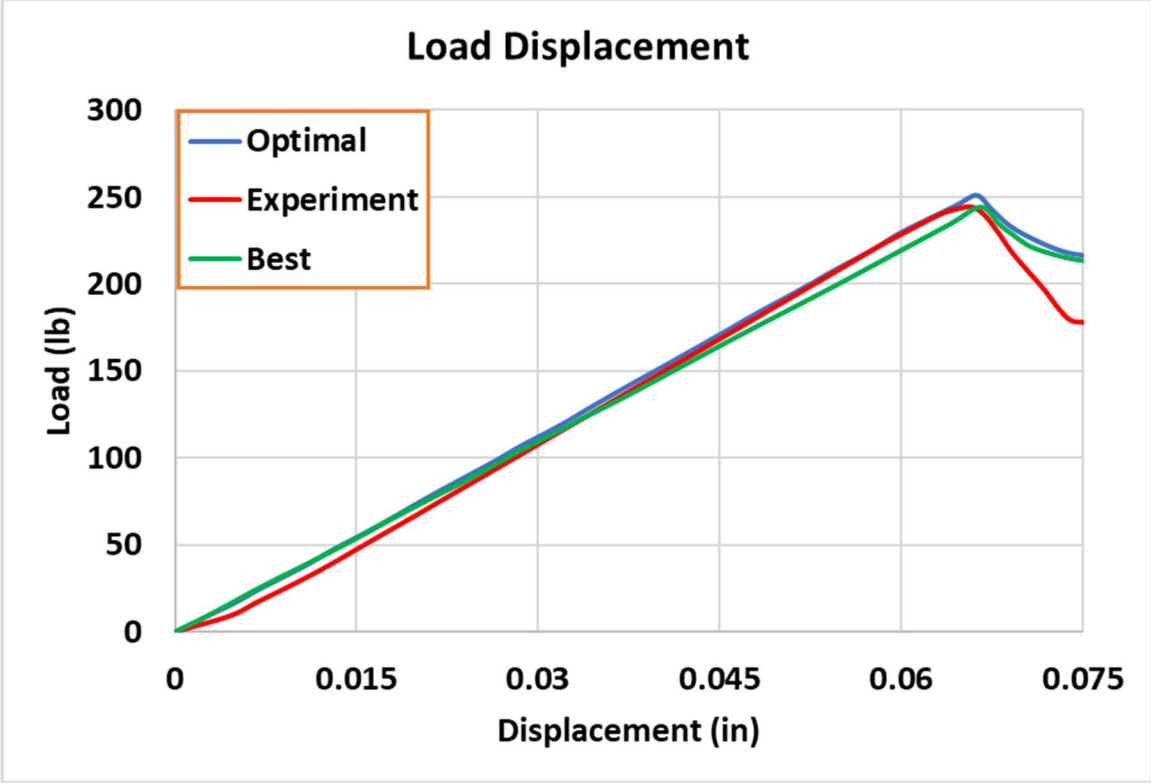

Figure 4.19. ENF Optimal Load Displacement Curve Compared with the Best and Experimental Results.

4.4. ANOVA ANALYSIS WITH DCB AND ENF TEST

Analysis of Variance (ANOVA) which is a robust statistical method, used here to obtain the important parameters and terms that significantly affect the traction separation law obtained from response surface methodology in previous section. To determine the effects of each parameter and their interaction on the traction separation law, a three-way ANOVA test was carried out using a combination of a full factorial and a polynomial of degree 2 model for both DCB and ENF tests. To conduct the three-way ANOVA test, the same set of data was used for response surface analysis given in Table 4.1 and Table 4.2. The ANOVA test was conducted on two separate instances. During the first instance (Analysis 1), all the necessary terms required for a complete factorial model along with a polynomial of degree 2 model was considered and all relevant terms were evaluated through ANOVA testing to determine significant factors. After identifying significant terms in the initial analysis and eliminating each insignificant term one at a time until all the remaining terms became significant, a second ANOVA test (Analysis 2) was conducted.

The data was analyzed in JMP Pro [25] using the least squares method, which is functionally equivalent to performing multiple linear regression. The majority of statistical methods employ the utilization of P-Value as a means of conducting hypothesis testing. The P-Value represents the likelihood of the null hypothesis being accurate, while the complementary probability of (1-the P-Value) indicates the probability of the alternative hypothesis being valid. Here, null hypothesis (H_0) and alternative hypothesis (H_1) are as follows-

H_0 : No effect of different input variables or parameters and their interactions on the output.

H_1 : Significant effect of different input variables or parameters and their interactions on the output.

So, smaller the p-values corresponding to any parameters represent more evidence that the null hypothesis is not true which means the effect of that parameter is significant on the output. The p-values are calculated by the F-distribution method which uses F-Value and corresponding degree of freedom of variables used in computing F-Value. F-Value of parameter "a" is computed by using Eqn. 4.12. All independent parameters were considered as continuous parameters in the analysis and the degree of freedom (D.O.F.) for continuous parameters is considered as 1. Table 5.1 has the degree of freedoms for both DCB and ENF tests. Most analysts consider statistically significant parameter if P-Value < 0.05 and statistically highly significant parameter if P-Value < 0.001.

Table 10. Degree of Freedom for Error from JMP Pro.

Test	Analysis 1	Analysis 2
DCB	16	21
ENF	12	16

$$\left(F-Value\right)_a = \frac{\left(Sum\ of\ \ Squares\ /\ D.O.F.\right)_a}{\left(Sum\ of\ \ Squares\ /\ D.O.F.\right)_{error}} \tag{4.12}$$

Table 5.2 and 5.3 has all the results from three-way ANOVA test for DCB and ENF test respectively. Based on the P-Value from analysis 1 of DCB test, significant terms were selected. Here, all the terms containing CTOD $\left(\delta_0\right)$ have P-Valve greater than 0.05 which is evident that CTOD does not play role of a significant parameter for DCB test.

Therefore, the terms containing δ_0 was removed from analysis 2. All terms have less than 0.05 P-Value in analysis 2 except the G_{IC} term. Term $\sigma^2_{\max,I}$ is significant and terms $\sigma_{\max,I}$, $G_{IC} \times \sigma_{\max,I}$ and G^2_{IC} are highly significant for the model to fit the DCB test data. After eliminating CTOD parameters, 3^2 design is sufficient for DCB test. Similarly, based on the P-Value from analysis 1 of ENF test, only terms $G_{IIC} \times \sigma_{\max,II}$ and G^2_{IIC} are significant. Therefore, the terms which are highly insignificant are eliminated one by one until all the remaining terms became significant. Thus, terms $\sigma_{\max,II}$, $\delta_{0,II}$, $G_{IIC} \times \sigma_{\max,II}$ and $\sigma_{\max,II} \times \delta_{0,II}$ are significant and term G^2_{IIC} is highly significant for the model to fit the ENF test data. After eliminating higher order insignificant terms, partial 3^k design is sufficient for ENF test. In both DCB and ENF test, term G_{IC} has P-Value greater than 0.05 but it is still not eliminated in the analysis 2. Because its higher order terms are significant and to consider the higher order terms in the analysis it is necessary to include all lower order terms.

Figures 5.1 and 5.2 shows the actual data point versus predicted values. Black dot points represent actual data points and red line shows the line of best fit from model and shaded area shows the 95% confidence interval region. The observed confidence interval for the ENF test exhibits a wider spread region in comparison to that of the DCB test, indicating that the model is a better fit for the DCB test as opposed to the ENF test. However, P-Value obtained from analysis 2 for both DCB and ENF test is below 0.001, indicating statistical significance.

Table 11. Effect Tests of Different Terms for DCB

Terms	Analysis 1			Analysis 2		
	Sum of Squares	F-Value	P-Value	Sum of Squares	F-Value	P-Value
G_{IC}	0.2877	3.6082	0.0757	0.2877	3.9868	0.0590
$\sigma_{\max,I}$	18.0915	226.8605	<0.0001	18.0915	250.6651	<0.0001
$\delta_{0,I}$	0.1749	2.1927	0.1581	-	-	-
$G_{IC} \times \sigma_{\max,I}$	1.9810	24.8410	<0.0001	1.9810	27.4476	<0.0001
$G_{IC} \times \delta_{0,I}$	0.0352	0.4414	0.5159	-	-	-
$\sigma_{\max,I} \times \delta_{0,I}$	0.0096	0.1202	0.7333	-	-	-
$G_{IC} \times \sigma_{\max,I} \times \delta_{0,I}$	0.0194	0.2433	0.6285	-	-	-
G_{IC}^2	46.4144	582.0170	<0.0001	46.4144	643.0884	<0.0001
$\sigma_{\max,I}^2$	0.5943	7.4522	0.0148	0.5943	8.2342	0.0092
$\delta_{0,I}^2$	0.0006	0.0081	0.9293	-	-	-
Error	1.2760	-	-	1.515658	-	-

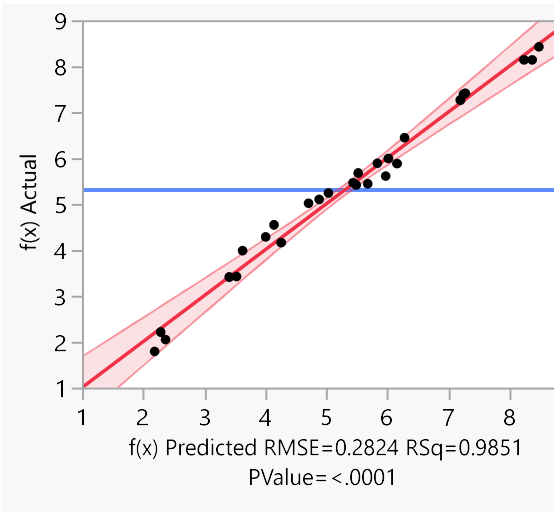

(a)

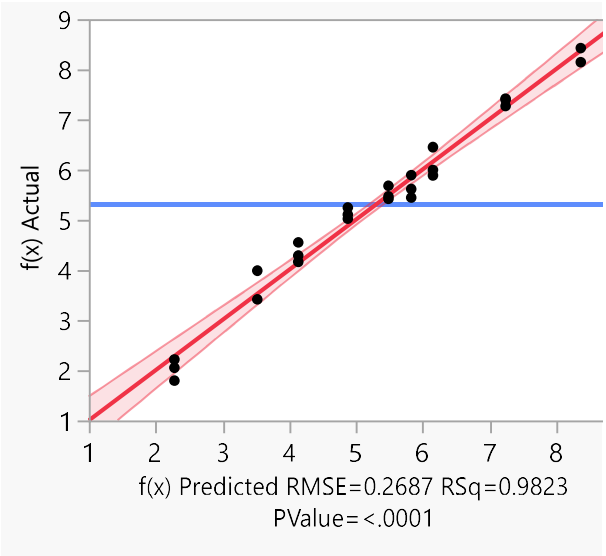

(b)

Figure 4.20. Actual f(x) data points with predicted f(x) for DCB test considering (a) Analysis 1 (b) Analysis 2.

Table 12. Effect Tests of Different Terms for ENF

Terms	**Analysis 1**			**Analysis 2**		
	Sum of Squares	**F-Value**	**P-Value**	**Sum of Squares**	**F-Value**	**P-Value**
G_{IIC}	141.1829	3.3051	0.0941	156.8309	3.9638	0.0639
$\sigma_{\max,II}$	152.5810	3.5720	0.0832	281.5371	7.1156	0.0169
$\delta_{0,II}$	192.0030	4.4948	0.0555	217.1659	5.4887	0.0324
$G_{IIC} \times \sigma_{\max,II}$	381.5401	8.9319	0.0113	426.6833	10.7841	0.0047
$G_{IIC} \times \delta_{0,II}$	68.2443	1.5976	0.2302	-	-	-
$\sigma_{\max,II} \times \delta_{0,II}$	180.3825	4.2228	0.0623	193.5674	4.8923	0.0419
$G_{IIC} \times \sigma_{\max,II} \times \delta_{0,II}$	0.9980	0.0234	0.8811	-	-	-
G_{IIC}^2	886.3676	20.7501	0.0007	1111.0593	28.0812	<0.0001
$\sigma_{\max,II}^2$	22.7433	0.5324	0.4796	-	-	-
$\delta_{0,II}^2$	1.0814	0.0253	0.8762	-	-	-
Error	512.5963	-	-	633.0562	-	-

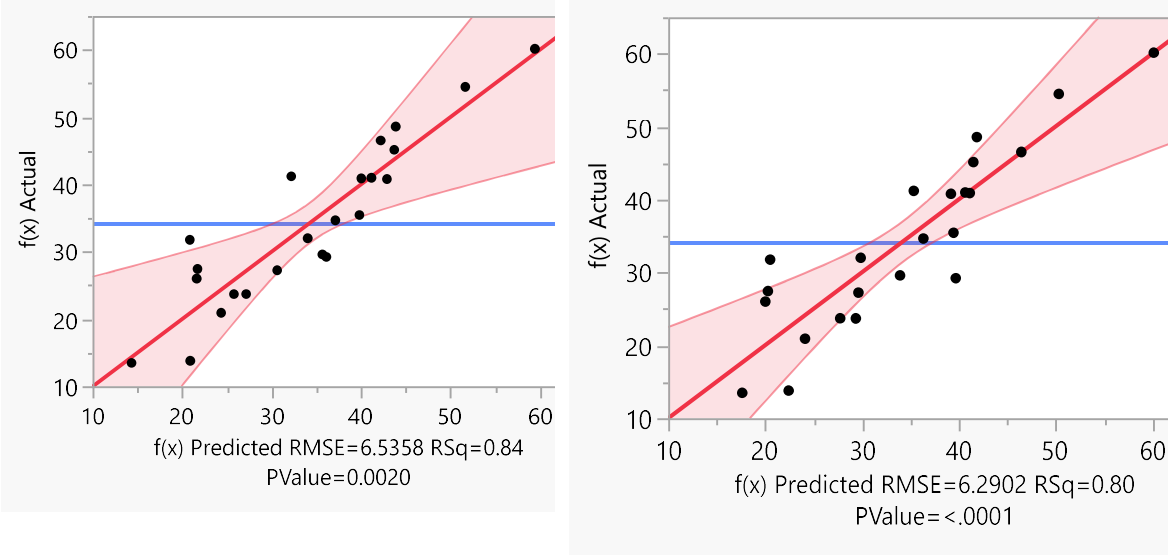

(a) (b)

Figure 4.21. Actual f(x) data points with predicted f(x) for ENF test considering (a) Analysis 1 (b) Analysis 2.

5. VALIDATION STUDY

5.1.1. QUAI-ISOTROPIC TENSION MODEL

Quasi-isotropic tension model refers to tension test performed on a composite laminate with a stacking sequence $45_2/90_4/-45_4/0_4$. The tested material is IM7-8552 unidirectional carbon/epoxy composite. The experiment was conducted by [29], and the resulting experimental curve was digitized for the purpose of comparing it to simulation results. A finite element model with a geometry of (120mm x 33mm x 5.26) is shown in Figure. 5.1.

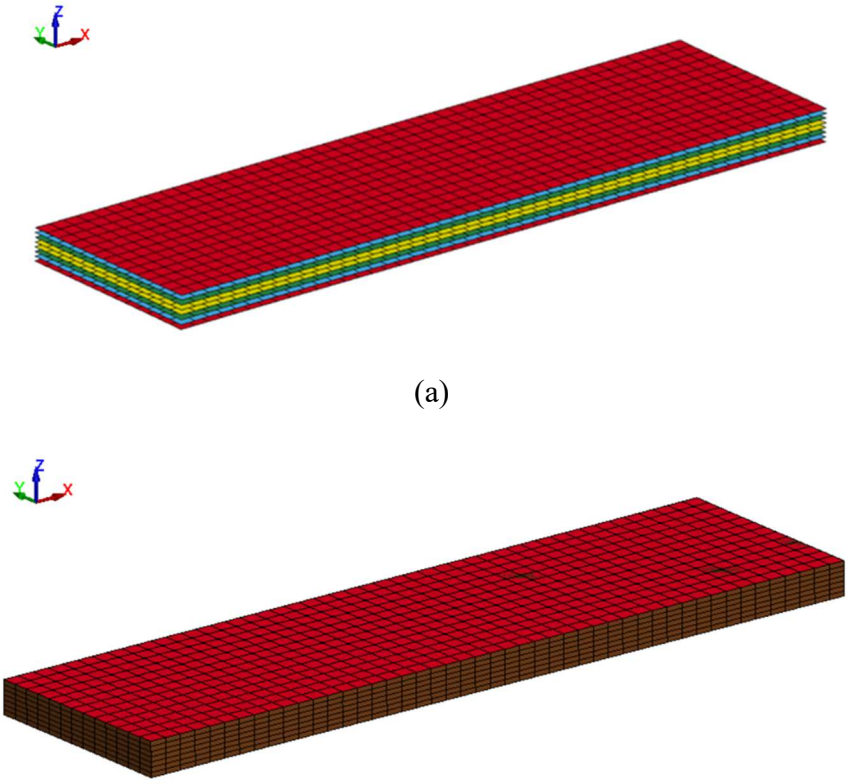

(a)

(b)

Figure 5.1. Quasi-Isotropic Tension Model, (a) Model Showing 8 Shell Layers (b) Model Showing Cohesive Zone Element In Between The Ply Layers

Finite Element Modeling: A total of eight shell layers was used to model the quasi-isotropic tension model. Each shell layer represents the four adjacent piles in the same direction. The thickness of shell layer was 0.72mm (corresponding to the total depth of four adjacent layers). The ply layers were modeled using fully integrated shell elements. The size of element was set to 2.54mm x 2.54mm based on the recommendations from [28]. The boundary conditions are as shown in Figure 5.1.2. Nodal displacements were applied to one edge of the specimen and the opposite edge of the specimen was constrained only in the loading direction. Figure 5.2 shows the applied displacements and boundary conditions. Red arrows represent the direction of applied displacement.

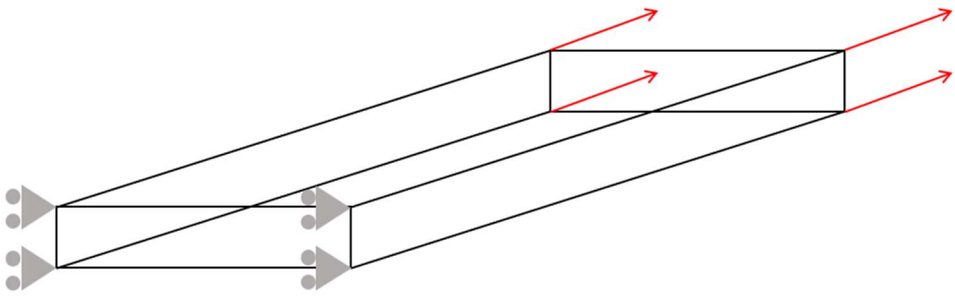

Figure 5.2 Quasi-Isotropic Tension Model Applied Displacement and Boundary Conditions

In the current study two quasi-isotropic models are analyzed. In the first model, tiebreak contact definition *CONTACT_AUTOMATIC_SURFACE_TO_SURFACE was defined between the plies to model delamination. In the second model, cohesive zone elements between the ply layers are used to model delamination using MAT_186. In both the models, MAT_213 was used to model the composite layers. In first model both the tiebreak parameters and MAT_213 input data was taken from [28]. In the second model, MAT_213 data generated in section 2 was used. The characterized mode I and mode II

fracture properties and traction separation laws characterized in chapter 4 were used as an input for MAT_186.

Results: The results from both the quasi-isotropic tension models are as shown in figure 5.3. The plot shows longitudinal stress – strain curves from both the models compared against the experimental curve taken from [29]. The longitudinal stress was computed using Eq. 5.1. Where F_R is reaction force at constrained nodes and A is the area of the specimen. Longitudinal strain was calculated using Eq. 5.2. where, ΔL is the change in length in the direction of the applied loading and L is the length of the specimen.

$$\sigma = \frac{\sum F_R}{A} \tag{5.1}$$

$$\varepsilon = \frac{\Delta L}{L} \tag{5.2}$$

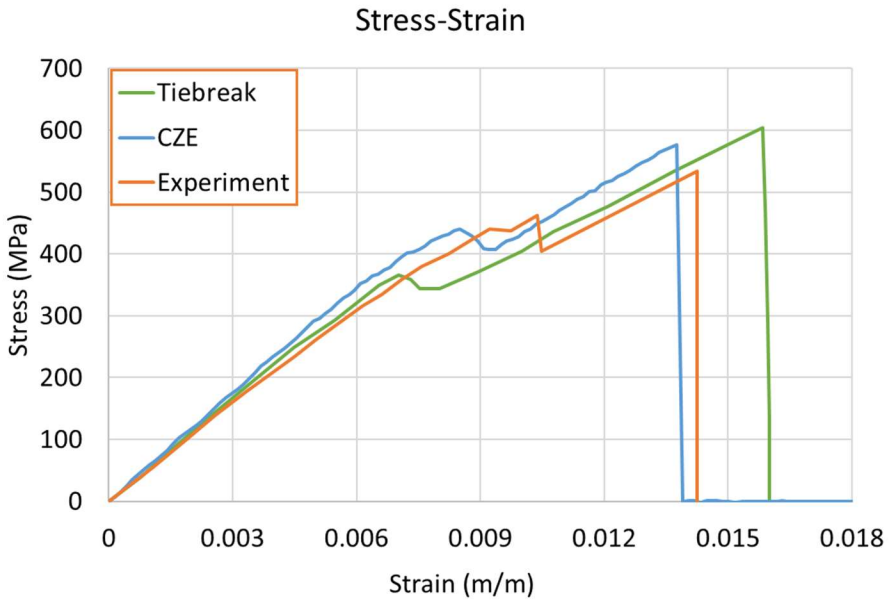

Figure 5.3. Simulated Stress-Strain Curve Compared Against the Experimental Curve

The initial effective modulus from both the models corresponds well with the experimental results. Delamination, which is the initial drop in the load, was better captured in the CZE model compared to tiebreak. Delamination stress for CZE model was around 440 MPa (versus 460 MPa in the experiment), while the tiebreak model recorded a delamination stress around 365 MPa. Wisnom et al [29] reported that delamination initiated between 45 and 90 degree plies that was also captured in the CZE model. While exact agreement between the experiment and the simulations stress strain curves from both the models was not observed, the initial linear behavior, initial delamination load drop followed by failure at a higher load was captured in both the models. Table 5.1 summarizes the key metrics of the stress-strain curves from Figure 5.3. '% Diff' refers to the percentage difference between the experiment and simulation.

Table 13. Key Features from Quasi-Isotropic Tension Model Simulation

	Initial Modulus		Delamination Initiation Stress		Failure Stress	
Model	Value (GPa)	% Diff	Value (MPa)	% Diff	Value (MPa)	% Diff
CZE	58.87	9.557%	440	-5.09%	572	6.87 %
Tiebreak	55.5	3.66%	365	-24%	604	12.33%

The results obtained from table 10 shows CZE model metrics have an error percentage less than ±10%. Typically this percentage error is considered acceptable for validation purposes [30]. It is worth mentioning that the exact match was not expected due to the use of plane stress elements instead of solid elements to have computational efficiency.

The table clearly indicates that results obtained from CZM (MAT_186), whose input was obtained from regression analysis done in chapter 4 works well when compared to the

tiebreak model whose input was obtained from post-processing DIC data from experiments.

6. CONCLUSIONS

Composites have many advantages over conventional materials due to their high specific strength, toughness, non-corrosiveness, and light weight. Therefore, they are widely used in aerospace and automotive applications. With the increasing use of composites there is also a need for a numerical tool that can be utilized in finite element simulations to predict the behavior of composites under dynamic loadings. Under the joint effort of NASA and FAA, an advanced orthotropic elasto-plastic damage material model (OEPDMM) is built and implemented in LS-DYNA, a commercially available nonlinear transient dynamic finite element code as MAT_213. This material model can predict linear and nonlinear deformations, damage, and failure in composite systems. MAT_213 has three sub models, that is deformation, damage, and failure. The model utilizes a generalized approach wherein no assumptions regarding the material behavior is made and tabulated input data in the form stress-strain curves obtained from quasi static room temperature (QS-RT) experiments. In this thesis a framework to generate the input for all deformation, damage and failure models is discussed including the computation of flow rule coefficients using MAT213 FRC computer program. To study the effects of the flow rule coefficients single element studies were performed by using T800-F3900 unidirectional carbon fiber -epoxy composite. The studies showed that even with different sets of FRC's, matching stress-strain curves were obtained. Characterized input data for IM7-8552 unidirectional carbon fiber-epoxy composite was used to build and analyze single element (SE) models. MAT_213 simulation stress-strain curves from SE models agreed with the user-defined input stress-strain curves. Hence, the generated input was compatible with MAT_213.

In addition to MAT_213 input data, the interlaminar properties for IM7-8552 composite required for MAT_186 cohesive zone model was characterized. MAT_186 input includes traction separation law (TSL) curves in both mode I and mode II fracture modes. Obtaining TSL solely from experiments requires close monitoring of the crack which is a tedious process to do even after using digital image correlation (DIC). A numerical inverse analysis method to precisely predict these parameters by using finite element analysis with cohesive zone modeling and response surface methodology (RSM) was used. Load displacement results from DCB and ENF experimental tests were used to compare with the DCB and ENF FE model results. The objective was to find the best combination of TSL parameters that enables the finite element analyses to fit the experimental load displacement curves. A nonlinear softening law was assumed for DCB to obtain mode I delamination cohesive law (TSL I). The law consists of an initial undamaged elastic response, followed by a non-linear softening branch. A nonlinear softening branch was used to account for the fiber bridging seen in the DCB experiments. Three parameters $G_{IC}, \sigma_{max,I}$ and $\delta_{0,I}$ (Critical energy release rate, peak traction and crack initiation CTOD) were used to define the mode I TSL law. In RSM, the root mean squared error between the FE and experimental load displacement curve was taken as an objective function. The objective function was then fitted with second order polynomial using Levenberg Marquardt Algorithm. Finally, the fitted equation was minimized to obtain optimal mode I fracture parameters. The optimal values for a $G_{IC}, \sigma_{max,I}$ and $\delta_{0,I}$ were 2.0534 (lb/in), 300 (psi), and 0.001935 (in) respectively. The FE load displacement result obtained using these parameters showed good agreement with the experimental load-displacement curve. A similar method using ENF model and experimental load

displacement curve along with RSM was followed to determine mode II traction separation law parameters. In the preliminary analysis, both linear and nonlinear softening laws were investigated for MAT_186 input in the ENF FE model. The results obtained showed little difference between the two softening laws. For simplicity purposes bilinear law was used. Similar to DCB, $G_{IIC}, \sigma_{max,II}$ and $\delta_{0,II}$ (Critical energy release rate, peak traction and crack initiation CTOD) was used to define the TSL. Root mean square error between the FE and experimental load displacement curve was used to define the objective function. Finally, the objective function was fitted with a second order polynomial in order to get a fitted function that was later minimized to obtain optimal mode II parameters. Optimal values for $G_{IIC}, \sigma_{max,II}$ and $\delta_{0,II}$was 5.32 (lb/in), 4198.4 (psi) and 0.001939 (in) respectively. The TSL generated from the optimal parameter had a longer hardening part compared to softening. During the preliminary ENF finite element simulations intended to determine the limits for fracture parameters, it was observed that certain combinations of fracture parameters produced favorable post-peak load displacement softening, but either underestimated or overestimated the initial stiffness and delamination initiation displacement. In contrast, combinations that produced better initial stiffness and delamination initiation displacement exhibited less post-peak softening than was observed experimentally. As a result, a decision had to be made, and the combinations that provided better delamination initiation displacement were chosen, as this measure is crucial when modeling delamination. Therefore, the optimal mode II combination resulted in satisfactory agreement between the FE and experimental load-displacement curves in the initial linear portion and delamination initiation displacement while underestimating the softening behavior.

Analysis of Variance (ANOVA) which is a robust statistical method, used here to obtain the important parameters and terms that significantly affect the traction separation law obtained from response surface methodology. A three-way ANOVA test was carried out using a combination of a full factorial and a polynomial of degree 2 model for both DCB and ENF tests. ANOVA analysis for DCB showed that the term containing CTOD (δ_0) did not have any significant effect. Whereas terms $\sigma_{\max,I}$, $G_{IC} \times \sigma_{\max,I}$ and G_{IC}^2 were highly significant for the model to fit the DCB test data. After eliminating the insignificant CTOD (δ_0) terms 3^2 design was sufficient for DCB test. In ENF test, terms $\sigma_{\max,II}$, $\delta_{0,II}$, $G_{IIC} \times \sigma_{\max,II}$ and $\sigma_{\max,II} \times \delta_{0,II}$ were significant and term G_{IIC}^2 was highly significant for the model to fit the ENF test data. After eliminating higher order insignificant terms, partial 3^k design was sufficient for ENF test.

In order to validate the optimal mode I and mode II fracture properties a quasi-isotropic tension test was performed using characterized data in a cohesive zone model (CZM), MAT_186 as an input to model delamination. The same model was also constructed using tiebreak to model delamination. The tiebreak input data was taken from Rudy Haluza's PhD dissertation [28] which was completely characterized by post processing the DCB and ENF experimental results. The simulation results from both the models showed that CZM model compared well with the experimental results across all validation metrics: The metrics evaluated for validation were initial modulus, delamination initiation stress and failure stress. Although the fracture properties obtained from the outlined procedure in this thesis show promising results, it may be necessary to re-adjust the parameters for varying loading conditions, which requires further

investigation. This can be achieved by performing crush or impact simulations by using cohesive zone modeling.

REFERENCES

[1] L. F. Alessandro Fascetti, “A critical review of numerical methods for the simulation of pultruded fiber-reinforced structural elements,” *Compos. Struct.*, vol. 273, p. 114284, Oct. 2021.

[2] M. F. S. F. de M. N.Dourado, “Bilinear approximations to the mode II delamination cohesive law using an inverse method,” vol. 49, pp. 42–50, Jun. 2012, doi: https://doi.org/10.1177/002199831244988.

[3] R. F. M.F.S.F. de Moura, “Mode II fracture characterization of a hybrid cork/carbon-epoxy laminate,” *Compos. Part B Eng.*, vol. 76, pp. 44–51, Jul. 2015, doi: https://doi.org/10.1016/j.compositesb.2015.02.010.

[4] R. P. Venkateswaran Shanmugam, “Stochastic modeling of delamination growth in unidirectional composite DCB specimens using cohesive zone models,” *Compos. Struct.*, vol. 102, pp. 36–60, Aug. 2013.

[5] M. J. M. S.M. Jensen and B. L. V. B. E. Lindgaard, “Inverse parameter identification of n-segmented multilinear cohesive laws using parametric finite element modeling,” *Compos. Struct.*, vol. 225, p. 111074, Oct. 2019.

[6] R. D. S. G. C. J.C.S. Azevedo and T. M. S. F. F.J.G. da Silva, “Cohesive law estimation of adhesive joints in mode II condition,” *Theor. Appl. Fract. Mech.*, vol. 80, pp. 143–154, 2015.

[7] L. S. Bilal M.Khaled and N. H. Subramaniam D. Rajan, “Enhancing the predictive capabilities of a composite plasticity model using cohesive zone modeling,” *Compos. Part Appl. Sci. Manuf.*, vol. 121, pp. 1–17, Jun. 2019, doi: https://doi.org/10.1016/j.compositesa.2019.03.001.

[8] ASTM D5528-13, “Standard test method for Mode I interlaminar fracture toughness of unidirectional fiber- reinforced polymer matrix composites.,” *ASTM Int.*, 2013.

[9] Martin, Roderick H and Murri, Gretchen B, “Characterization of Mode 1 and Mode 2 delamination growth and thresholds in graphite/peek composites.” NASA Langley Research Center, Hampton, VA, 1988.

[10] Yong Zhu, Kenneth M. Liechti, and K. Ravi-Chandar, “Direct extraction of rate-dependent traction–separation laws for polyurea/steel interfaces,” *Int. J. Solids Struct.*, vol. 46, no. 1, pp. 31–51, 2009.

[11] Ainhoa Arrese, Ana Boyano, Juan De Gracia, and Faustino Mujika, “A novel procedure to determine the cohesive law in DCB tests,” *Compos. Sci. Technol.*, vol. 152, 2017, doi: https://doi.org/10.1016/j.compscitech.2017.09.012.

[12] M. F. S. F. de M. F.A.M. Pereira, “Determination of mode II cohesive law of bovine cortical bone using direct and inverse methods,” *Int. J. Mech. Sci.*, vol. 138–139, pp. 448–456, 2018.

[13] Y. L. Eu-Tteum Park, “Inverse analysis on mode II adhesive properties of PP film in fiber metal laminate using hybrid Levenberg–Marquardt methods,” *Adv. Compos. Mater.*, vol. 30, pp. 570–590, Apr. 2021, doi: https://doi.org/10.1080/09243046.2021.1911498.

[14] Robert K. Goldberg *et al.*, “Development of an Orthotropic Elasto-Plastic Generalized Composite Material Model Suitable for Impact Problems,” *J. Aerosp. Eng.*, vol. 29, no. 4, Jul. 2016, doi: https://doi.org/10.1061/(ASCE)AS.1943-5525.0000580.

[15] Canio Hoffarth *et al.*, “Implementation and validation of a three-dimensional plasticity-based deformation model for orthotropic composites,” *Compos. Part Appl. Sci. Manuf.*, vol. 91, no. 1, pp. 336–350, Dec. 2016, doi: https://doi.org/10.1016/j.compositesa.2016.10.024.

[16] Canio Hoffarth *et al.*, “Verification and Validation of a Three-Dimensional Orthotropic Plasticity Constitutive Model Using a Unidirectional Composite,” *fibers*, vol. 5, no. 1, doi: https://doi.org/10.3390/fib5010012.

[17] Bilal Khaled *et al.*, “Damage characterization of composites to support an orthotropic plasticity material model,” *J. Compos. Mater.*, vol. 53, no. 7, pp. 941–967, doi: DOI: 10.1177/0021998318793506.

[18] Loukham Shyamsunder *et al.*, “Implementing deformation, damage, and failure in an orthotropic plastic material model,” *J. Compos. Mater.*, vol. 0, no. 0, pp. 1–22, 2019, doi: DOI: 10.1177/0021998319865006.

[19] Loukham Shyamsunder, Bilal Khaled, Subramaniam D Rajan, and Gunther Blankenhorn, “Improving failure sub-models in an orthotropic plasticity-based material model,” vol. 55, no. 15, pp. 2025–2042, 2021, doi: DOI: 10.1177/0021998320982651.

[20] Hoffarth C, “A generalized orthotropic elasto-plastic material model for impact analysis. (Doctoral dissertation) Arizona State University.” 2016.

[21] Shyamsunder L, “Failure modeling in an orthotropic plastic material model under static and impact loading (Doctoral dissertation) Arizona State University.” 2020.

[22] Stephen W. Tsai and Edward M. Wu, “A General Theory of Strength for Anisotropic Materials,” *J. Compos. Mater.*, vol. 5, no. 1, doi: https://doi.org/10.1177/002199837100500106.

[23] A. Puck and H. Schürmann, “Failure analysis of FRP laminates by means of physically based phenomenological models,” *Chapter 56 - Fail. Criteria Fibre-Reinf.-Polym. Compos.*, pp. 832–876, 2004, doi: https://doi.org/10.1016/B978-008044475-8/50028-7.

[24] Alan Arnold Griffith, “The phenomena of rupture and flow in solids,” *R. Soc.*, vol. 221, no. 582–593, 1921, doi: https://doi.org/10.1098/rsta.1921.0006.

[25] D.S. Dugdale, “Yielding of steel sheets containing slits,” *J. Mech. Phys. Solids*, vol. 8, no. 2, pp. 100–104, May 1960, doi: https://doi.org/10.1016/0022-5096(60)90013-2.

[26] G.I. Barenblatt, “The Mathematical Theory of Equilibrium Cracks in Brittle Fracture,” *Adv. Appl. Mech.*, vol. 7, pp. 55–129, 1962, doi: https://doi.org/10.1016/S0065-2156(08)70121-2.

[27] Dr. Subramaniam Rajan, “MAT213 Flow Rule Coefficients Program Guide.”

[28] Rudy Haluza, “Measurement And Explicit Finite Element Modeling Of Dynamic Crush Behavior Of Carbon Fiber Reinforced Polymer Composites (Doctoral Dessertation).” Dec. 2022.

[29] M.R. Wisnom, B. Khan, and S.R. Hallett, “Size effects in unnotched tensile strength of unidirectional and quasi-isotropic carbon/epoxy composites,” *Compos. Struct.*, vol. 84, no. 1, pp. 21–28, Jun. 2008.

[30] Ali Rabiee and Hessam Ghasemnejad, “Finite Element Modelling Approach for Progressive Crushing of Composite Tubular Absorbers in LS-DYNA: Review and Findings,” *J. Compos. Sci.*, vol. 6, no. 1, 2022, doi: https://doi.org/10.3390/jcs6010011.

[31] A. K. Amirali Khosrozadeh, “Inverse identification of material constants of various cohesive laws for delamination of composites using experimental results,” *Compos. Struct.*, vol. 303, Jan. 2023, doi: https://doi.org/10.1016/j.compstruct.2022.116241.

[32] Y. D. Zhi ZAN and F. Q. Shuai ZHAO, “CZM determination and numerical analysis on interface delamination of nickel coated carbon nanotubes reinforced sintered silver interconnection layers,” *IEEE*, Sep. 2022, doi: 10.1109/ICEPT56209.2022.9873154.

[33] Leo Škec, “Identification of parameters of a bi-linear cohesive-zone model using analytical solutions for mode-I delamination,” *Eng. Fract. Mech.*, vol. 214, pp. 558–577, Jun. 2019, doi: https://doi.org/10.1016/j.engfracmech.2019.04.019.

[34] N. I. A.Arrese, M. P.-G. F. Mujika, and J. Renart, “A novel experimental procedure to determine the cohesive law in ENF tests,” *Compos. Sci. Technol.*, vol. 170, pp. 42–50, Jan. 2019, doi: https://doi.org/10.1016/j.compscitech.2018.11.031.

[35] ASTM D7905/D7905M-14, “Standard test method for Mode II interlaminar fracture toughness of unidirectional fiber-reinforced polymer matrix composites.,” *ASTM Int.*, 2014.

[36] T. C. MinJung Lee, B. L. WonSeock Kim, and JungJu Lee, “Determination of cohesive parameters for a mixed-mode cohesive zone model,” vol. 30, 2010, doi: https://doi.org/10.1016/j.ijadhadh.2009.10.005.

[37] S. P. T. Ashutosh Maurya and Subramaniam Rajan, “Experimental Tests to Characterize the Behavior and Properties of IM7-8552 Composite,” Jan. 2023.

[38] A. B. P. A.B. de Morais, “Application of the effective crack method to mode I and mode II interlaminar fracture of carbon/epoxy unidirectional laminates,” *Compos. Part Appl. Sci. Manuf.*, vol. Volume 38, no. Issue 3, pp. 785–794, Mar. 2007, doi: https://doi.org/10.1016/j.compositesa.2006.09.001.

[39] Khaled B, “Experimental characterization and finite element modeling of composites to support a generalized orthotropic elasto-plastic damage material model for impact analysis (Doctoral dissertation) Arizona State University.” 2019.

[40] Ashutosh Maurya, Seetha Pavan Tanneru, Subramaniam Rajan, J. Michael Pereira, and Sandi G. Miller, “Experimental Tests to Characterize the Behavior and Properties of IM7-8552 Composite.” NASA/TM-20230001560.

[41] L.A. Carlsson, J.W. Gillespie, and R.B. Pipes, “On the Analysis and Design of the End Notched Flexure (ENF) Specimen for Mode II Testing,” *J. Compos. Mater.*, vol. 20, no. 6, 1986, doi: 10.1177/002199838602000606.